

AGN activity and the misaligned hot ISM in the compact radio elliptical NGC4278

S. Pellegrini¹, J. Wang², G. Fabbiano², D.W. Kim², N.J. Brassington³, J.S. Gallagher⁴, G. Trinchieri⁵, A. Zezas⁶

¹*Department of Astronomy, University of Bologna, via Ranzani 1, 40127 Bologna, Italy*

²*Harvard-Smithsonian Center for Astrophysics, 60 Garden St, Cambridge, MA 02138, USA*

³*School of Physics, Astronomy and Mathematics, University of Hertfordshire, Hatfield, UK*

⁴*Department of Astronomy, University of Wisconsin-Madison, Madison, WI 53706, USA*

⁵*INAF-Osservatorio Astronomico di Brera, Via Brera 28, 20121 Milano, Italy*

⁶*Physics Department, University of Crete, Heraklion, Greece*

ABSTRACT

The analysis of a deep (579 ks) *Chandra* ACIS pointing of the elliptical galaxy NGC4278, which hosts a low luminosity AGN and compact radio emission, allowed us to detect extended emission from hot gas out to a radius of ~ 5 kpc, with 0.5–8 keV luminosity of 2.4×10^{39} erg s⁻¹. The emission is elongated in the NE-SW direction, misaligned with respect to the stellar body, and aligned with the ionized gas, and with the *Spitzer* IRAC 8 μ m non-stellar emission. The nuclear X-ray luminosity decreased by a factor of ~ 18 since the first *Chandra* observation in 2005, a dimming that enabled the detection of hot gas even at the position of the nucleus. Both in the projected and deprojected profiles, the gas shows a significantly larger temperature ($kT = 0.75$ keV) in the inner ~ 300 pc than in the surrounding region, where it stays at ~ 0.3 keV, a value lower than expected from standard gas heating assumptions. The nuclear X-ray emission is consistent with that of a low radiative efficiency accretion flow, accreting mass at a rate close to the Bondi one; estimates of the power of the nuclear jets require that the accretion rate is not largely reduced with respect to the Bondi rate. Among possible origins for the central large hot gas temperature, such as gravitational heating from the central massive black hole and a recent AGN outburst, the interaction with the nuclear jets seems more likely, especially if the latter remain confined, and heat the nuclear region frequently. The unusual hot gas distribution on the galactic scale could be due to the accreting cold gas triggering the cooling of the hot phase, a process also contributing to the observed

line emission from ionized gas, and to the hot gas temperature being lower than expected; alternatively, the latter could be due to an efficiency of the type Ia supernova energy mixing lower than usually adopted.

Subject headings: galaxies: elliptical and lenticular, CD – galaxies: individual: NGC4278 – galaxies: active – galaxies: nuclei — X-rays: galaxies — X-rays: ISM

1. Introduction

In recent years, high angular resolution X-ray observations of early type galaxies performed with *Chandra* allowed us to investigate extensively the connection between the central supermassive black hole (MBH) and the surrounding hot interstellar medium (ISM; e.g., Forman et al. 2007, Allen et al. 2006, Diehl & Statler 2008, David et al. 2009, Million et al. 2010), a study with important implications for the building of a complete picture of the host galaxy–MBH coevolution (Silk & Rees 1998, Di Matteo, Springel & Hernquist 2005, Hopkins et al. 2005, Merloni & Heinz 2008, Cattaneo et al. 2009, Schawinski et al. 2009, Johansson et al. 2009, Ciotti et al. 2010, Kaviraj et al. 2011). The investigations so far concentrated mostly on X-ray bright and massive ellipticals, where the high hot gas surface brightness most clearly reveals signs of feedback heating as cavities, shells, filaments, and edges. For a complete understanding of the MBH-host galaxy coevolution process, it is however important to realize how the activity cycle works even in low to intermediate mass galaxies, which are far more numerous, and currently almost unexplored. Other aspects still unclear include the relationship between the nuclear emission and other galactic properties, as the fuel availability for the MBH (e.g., Ho 2008, Pellegrini 2010, Gallo et al. 2010); the accretion modalities [standard disk plus hot corona, Haardt & Maraschi (1993); or radiatively inefficient accretion, RIAF, Narayan & Yi (1995); e.g., Ptak et al. 2004, Maoz 2007, Ho 2008]; and what determines the partition in the accretion output between radiative and mechanical energies (e.g., Allen et al. 2006, Merloni & Heinz 2007).

In this paper we analyze two new *Chandra* pointings of the medium-mass elliptical galaxy NGC4278 ($d = 16.1$ Mpc¹, and $L_B = 1.7 \times 10^{10} L_{B,\odot}$; Tab. 1), obtained in March 2010; we also consider the data of 6 previous pointings between 2005 and 2007, totalizing 579 ks of net exposure time. With this deep observation we explore the origin of the nuclear emission and the possible interaction of the AGN activity with the surrounding hot ISM.

¹At this distance $1'' = 78$ pc.

The spatially resolved properties of the low surface brightness hot gas could be determined at a high level of accuracy thanks to the long exposure time, the careful subtraction of the emission from stellar sources allowed for by the *Chandra* high angular resolution, and the significant dimming of the nucleus during year 2010; all this has allowed us to determine the gas properties of the central region (down to within a radius of $2''$ from the nucleus) and of the more extended galactic body, out to a radius of $\sim 70''$ (~ 5 kpc).

NGC4278 is a relatively isolated elliptical galaxy, belonging to the LGG 279 group of 17 galaxies (Garcia 1993); its morphological type is E1-2, it has a regular optical shape, and a uniformly old stellar population (Shapiro et al. 2010, Kuntschner et al. 2010). NGC4278 also hosts a LINER1 nucleus, with a weak broad component in the optical $H\alpha$ line (Ho et al. 1997). Unlike standard AGNs, NGC4278 shows an X-ray nuclear emission of low level ($\sim 10^{40}$ erg s^{-1} ; Younes et al. 2010), and a very sub-Eddington bolometric emission (5×10^{-6} , Eracleous et al. 2010a, Nemmen et al. 2011). This LINER is known to be radio-loud (Terashima & Wilson 2003), and has been deeply studied in the radio. At arcsecond resolution, the VLA shows an unresolved emission from 5 to 43 GHz (Wrobel & Heeschen 1984, Nagar et al. 2001), while an extended structure is visible at milliarcsecond resolution with the VLBI at 18 and 6 cm (Schilizzi et al. 1983), and a parsec-scale two-sided radio jet was resolved by the VLBA emerging from a central compact component (Giroletti et al. 2005). The highly bent jet morphology suggests that the jet may be interacting with the ambient medium in the inner few parsecs. The total radio (VLA) luminosity is $P_{1.4GHz} = 1.0 \times 10^{21.7}$ W Hz^{-1} (Giroletti et al. 2005, for our adopted distance), and then at least 2 orders of magnitude lower than in powerful radio-loud AGN.

NGC4278 finally hosts a multiphase interstellar medium. The SAURON survey (Sarzi et al. 2006) revealed strong emission from ionized gas in the central region, whose kinematical structure is consistent with that inferred for a massive ($M_{HI} = 6.9 \times 10^8 M_{\odot}$), extended (with a diameter of 37 kpc), and regular HI disk (Raimond et al. 1981, Morganti et al. 2006). CO emission was not detected and an upper limit to the molecular gas mass of $M_{H_2} < 6.9 \times 10^6 M_{\odot}$ was placed (Crocker et al. 2011). Recently, Tang et al. (2011) presented mid-infrared emission maps of the extended ionized gas, the warm molecular hydrogen and the dust, using *Spitzer* spectroscopic observations.

In this paper we present the deep *Chandra* observations and their imaging and spectral analysis in Sects. 2, 3 and 4; we summarize the observational results in Sect. 5, discussing next the origin of the nuclear emission (Sect. 5.1), that of the hot gas discovered at the nucleus (Sect. 5.2), and the relationship between the various gas phases (Sect. 5.3). We finally present our conclusions in Sect. 6.

2. Observations and data analysis

We utilized 6 archival and 2 new *Chandra* observations of NGC 4278, imaged with the S3 chip of *Chandra* Advanced CCD Imaging Spectrometer (ACIS; Garmire et al. 2003). The two recent observations (PI: Fabbiano) were taken on March 15, 2010 (obsID 11269) and March 20, 2010 (obsID 12124), with exposure times of 81.9 ks and 25.8 ks, respectively.

We reduced and analyzed the observational data using the *Chandra* Interactive Analysis of Observations (CIAO) tools². The CIAO script CHANDRA_REPRO was used to reprocess all data with the latest calibration, remove pixel randomization, and apply the sub-pixel (“EDSER”) algorithm. We reprojected the event lists to obsID 11269 and merged the observations to create a master event file and the associated exposure map using MERGE_ALL. After a thorough source searching with WAVDETECT (Freeman et al. 2002) using all 8 co-added observations, 251 X-ray point sources were found. Details of the procedures performed to detect point sources were reported in Brassington et al. (2009) and Fabbiano et al. (2010).

From the co-added data set, *Chandra* images in 0.3-0.9 keV (“soft band”), 0.9-2.5 keV (“medium band”), and 2.5-8.0 keV (“hard band”) were created and adaptively smoothed using the CIAO task *csmooth*; the smoothing kernel was constrained to yield a minimum signal-to-noise ratio (S/N) of 2.5σ and a maximum of 5σ . An X-ray “false color” image was created by combining these three smoothed and exposure corrected images shown in red, green, and blue, respectively (Figs. 1a and 1b).

To study the extended emission, we first masked out all point sources using apertures with $2''$ radii, corresponding to $\approx 95\%$ PSF encircled-energy radius at 1.496 keV. The resulting “swiss cheese” image should include a minimum contribution from detected point sources. The spectral extraction was done with the CIAO script *specextract*³, which creates area-weighted Response Matrix Files (RMF) and Ancillary Response Files (ARF) for each region in individual observations. Background counts were taken from an annulus of source-free region between $r = 100''$ and $r = 120''$ (see Sect. 3.1 on determining the extent of the diffuse emission), and within the ACIS-S3 chip in all observations. For each region of interest, source spectra were grouped to a minimum of 15 counts per bin to allow spectral fitting with χ^2 -statistic.

The extracted spectra were modelled with XSPEC v12.7.0, using combinations of an absorbed optically-thin thermal emission (APEC model, Smith et al. 2001) and power law

²See <http://cxc.harvard.edu/ciao/> for details on CIAO.

³See CIAO thread <http://cxc.harvard.edu/ciao/threads/specextract/>.

components. A single line-of-sight absorption column N_H was used in all cases, allowed to vary freely. When the fit required a very small absorption ($N_H \ll 10^{20} \text{ cm}^{-2}$), N_H was frozen at the Galactic column towards NGC 4278 ($1.76 \times 10^{20} \text{ cm}^{-2}$; from CXC tool COLDEN⁴). The spectral modeling was done using the full 0.3–8.0 keV energy range. In the thermal APEC model, the abundance was fixed to solar, with the abundance table from Anders & Grevesse (1989).

3. Imaging Analysis

3.1. The X-ray Morphology

Figure 1a gives the $4' \times 4'$ view of the X-ray emission of NGC 4278. The bright nucleus and the point sources are clearly visible (not removed). There is extended emission in the inner $30''$, with a clear elongation along the northeast (NE; top-left) and the southwest (SW; lower right) direction. Figure 1b zooms in to the central $70''$ -across (~ 5.5 kpc) region, and Fig. 1c shows the 0.3–2 keV emission in the innermost $20''$ region. An extended feature is present SW of the nucleus, but not seen in other wavelengths when available images in the literature were examined.

Figure 2a shows the azimuthally averaged radial profile of the extended X-ray emission in the 0.3–0.9 keV energy band, which emphasizes the hot ISM presence, since harder emission mostly arises from unresolved stellar sources as binaries. We have excluded all detected sources (as explained above), and centered the concentric annuli in steps of $5''$ on the nucleus, identified as the optical/IR peak. The raw profile flattens at a radius of $\sim 70''$, where the field background starts dominating. We therefore used the $100''$ – $140''$ region to measure the local background and subtract it from the emission, to produce the net profile. We further extracted counts from every 10° -wide sectors, extending from $2''$ to $60''$, to create an azimuthal distribution for the extended soft X-ray emission; this procedure identifies sectors that contain brighter emission (Fig. 2b), and the results were used to guide the choice of regions for the spectral extraction (see Sect 4.2).

In Fig. 2c we show the background subtracted radial profiles of the extended emission along two directions, the NE–SW sector which contains the X-ray brighter quadrants towards NE (position angle [P.A.] ranging between 20° and 110° , counterclockwise from N) and SW (P.A. from 180° to 290°), and the NW–SE sector which contains the NW (P.A. from 290° to 20°) and SE (P.A. from 110° to 180°) quadrants. The radial profiles in the optical I-band

⁴<http://cxc.harvard.edu/toolkit/colden.jsp>

from Cappellari et al. (2006) and in the near-IR K band from the Two Micron All Sky Survey (2MASS) Large Galaxy Atlas (Jarrett et al. 2003) are also shown for a comparison with the stellar light distribution. The soft X-ray profile of the NE-SW emission is clearly higher than that of the NW-SE emission within a radius $r \sim 20''$; both emissions follow the optical/IR light profile at $r > 30''$, while they are steeper than that, inner of $r = 20''$. The separate brightness profiles of the brighter NE and SW quadrants closely follow each other, and are not shown here; the separate profiles of the fainter NW and SE quadrants are also consistent with each other, though with lower statistics.

Having established the presence, extent and elongation of the soft X-ray emission, we next turned to investigate the possible presence of features in the soft X-ray morphology. We first modeled the extended soft emission (point source removed and filled) within a radius of $r = 50''$ with a smooth 1-D β -model using CIAO’s modeling and fitting package **Sherpa**⁵ (Doe et al. 2007). Clear elongation along the NE-SW direction is seen in the residual image, as expected given that the profile in this direction keeps higher than that along the NW-SE (see Fig. 2); thus, a 2-D (elliptical) β -model was adopted. Full description of the model is available at <http://cxc.harvard.edu/sherpa/ahelp/beta2d.html>. The center of the model image was fixed at the location of the peak intensity of the X-ray image (x_0, y_0) , and the modeling included a central point source plus a smooth extended emission, described by a 2-D Lorentz model with a varying power law, known as a 2-D beta model:

$$f(x, y) = A * (1 + [r(x, y)/r_0]^2)^{-\alpha} \quad (1)$$

where $r(x, y) = \sqrt{x_1^2(1 - \epsilon)^2 + y_1^2}/(1 - \epsilon)$, $x_1 = (x - x_o)\cos\theta + (y - y_o)\sin\theta$ and $y_1 = (y - y_o)\cos\theta - (x - x_o)\sin\theta$, and θ is the position angle of the major axis of the ellipse. The model was blurred by a kernel representing the PSF in the image fitting⁶. The best fit parameter values were $r_0 = 0.87'' \pm 0.05$ for the core radius, $\theta = 261^\circ \pm 5^\circ$, $\epsilon = 0.17 \pm 0.01$ for the ellipticity, and $\alpha = 1.1 \pm 0.01$. Figure 3 shows the ratio image between the background subtracted soft X-ray emission and the 2D model image (without including the bright nucleus in the model). Only features with a minimum significance of 2.5σ are shown. The point sources were retained to outline their spatial distribution with respect to the residual features. Along the NE-SW direction there are prominent clumps of emission, that are likely responsible for the excess in the radial profile plots along this direction (Figs. 2b and 2c). There is also a deficit of emission immediately SW of the nucleus. The overall morphology is that of an elongated elliptical shape, with an irregular distribution of clumps and deficits within it.

⁵<http://cxc.harvard.edu/sherpa4.4/>

⁶See the CIAO thread <http://cxc.harvard.edu/sherpa/threads/2dpsf/>.

3.2. Comparison with Multiwavelength Maps

Figure 4 compares the contours of the extended X-ray emission in the 0.3–0.9 keV band with the HST WFPC2 V band image (Carollo et al. 1997), *Spitzer* IRAC $8\mu\text{m}$ emission (with stellar continuum removed; Tang et al. 2011), and the ionized gas maps ([OIII], $\text{H}\beta$ emission, [OIII]/ $\text{H}\beta$, $\text{EW}_{[\text{OIII}]}$) from the SAURON survey (Sarzi et al. 2006). In each panel, we also show (1) the directions of the two-sided pc-scale radio jet, (2) the major axis of the optical isophote, and the rotation axis of the stars in the inner galactic region; and (3) the rotation axis for the ionized gas (Sarzi et al. 2006; see also Morganti et al. 2006). Note how the isophotes of the stars and of the ionized gas are oriented differently, and how stars and ionized gas rotate about two slightly misaligned axes (Sarzi et al. 2006). The hot gas is clearly elongated but misaligned with the optical stellar body of the galaxy, and it follows more closely the ionized gas distribution and the *Spitzer* IRAC $8\mu\text{m}$ emission.

4. Spectral Analysis

4.1. The X-ray Nucleus

The X-ray emission from the nuclear source was studied by Younes et al. (2010), based on the *Chandra* pointings prior to March 2010, and an *XMM – Newton* pointing of 2004. In their results (see their Table 2), the 0.5–8 keV flux varies from 6×10^{-13} to 1.8×10^{-12} $\text{erg cm}^{-2} \text{s}^{-1}$. We have examined these previous data using a different approach by directly applying the pileup model of Davis (2001), and we confirm the Younes et al.’s results. We study here the nuclear emission, focussing on the new data. During the two observations acquired in 2010, the count rate was 0.06 per ACIS frame, and the photon pile-up was negligible ($< 2\%$), in contrast to the high pile-up fraction ($\sim 5\%–20\%$) when the nucleus was seen at a higher flux (Younes et al. 2010). The nucleus appears to be in its lowest flux state during the 2010 observations (Tab. 2).

The nuclear spectra from the last two observations were extracted from a $2''$ radius circular aperture, and were fitted jointly (Fig. 5). An absorbed power-law model gave no acceptable fit (reduced $\chi^2 = 2.8$), in contrast with the highest flux state case (ObsID 4741), where a simple power law with photon index $\Gamma = 2$ could fit the nuclear spectrum. The 0.3–2 keV band shows residuals around ~ 1 keV, strongly suggesting the presence of emission from hot gas. The addition of a thermal component (*APEC* model) takes into account these residuals in the soft band, and significantly improves the fit quality (at $> 99.9\%$ confidence level, as established by the F-test). The best fit temperature is $kT = 0.75 \pm 0.05$ keV and the power law $\Gamma = 2.31 \pm 0.20$. The quoted errors are 90% confidence intervals for one

interesting parameter. The observed total nuclear flux is $F_{0.5-8keV} = 1.02_{-0.17}^{+0.11} \times 10^{-13}$ erg cm^{-2} s^{-1} , and $F_{0.5-8keV} = 1.1 \pm 0.2 \times 10^{-13}$ erg cm^{-2} s^{-1} after correction for absorption ($N_H = 4.18 \pm 3.13 \times 10^{20}$). We also attempted to fit the two observations individually, and found $F_{0.5-8keV} = 1.17 \pm 0.05 \times 10^{-13}$ erg cm^{-2} s^{-1} for ObsId 11269 and $F_{0.5-8keV} = 0.95 \pm 0.08 \times 10^{-13}$ erg cm^{-2} s^{-1} for ObsId 12124 (both absorption corrected); the nuclear flux is slightly lower in the latter observation. In any case, the flux was a factor of 18 lower than the highest flux reported in Younes et al. (2010). The comparison with the Younes et al. (2010) results is summarized in Table 2. The nuclear luminosity due to the power law component is $L_{0.5-8keV} = 2.5 \times 10^{39}$ erg s^{-1} ; Tab. 3 gives the luminosities of the thermal and power law components in various bands.

The thermal component alone has $L_{0.5-2keV} = 9.9 \times 10^{38}$ erg s^{-1} (absorption corrected), and accounts for 40% of the total 0.5–2 keV emission within the $R = 2''$ region ($L_{0.5-2keV} = 2.5 \times 10^{39}$ erg s^{-1} , absorption corrected; Tab. 3). We can rule out the possibility that a significant fraction of the thermal emission at the nucleus position is originated from the combined contribution from the AB+CV stellar population (e.g., Boroson et al. 2011; see also Sect. 4.2 below), since the latter is estimated to account for only $\sim 0.5\%$ of the 0.5–2 keV hot gas emission in the extraction region. This estimate is based on the 2MASS K-band image, which gives a K-band luminosity of $1.0 \times 10^9 L_{K,\odot}$ for the region used for the extraction of the nuclear spectrum (for $M_{K,\odot} = 3.3$ mag). Adopting the $L_{0.5-2keV}/L_K = 4.4 \times 10^{27}$ erg $\text{s}^{-1}/L_{K,\odot}$ conversion relation for the AB+CV emission (eq. A1 in Boroson et al. 2011), this gives a stellar AB+CV luminosity of $L_{0.5-2keV} = 4 \times 10^{36}$ erg s^{-1} .

4.2. The extended emission

We derived the temperature and density profiles of the hot gas using all available *Chandra* ObsIDs. Due to statistics, to obtain enough counts, we analyzed the combined spectra extracted from radial bins along two directions, the NE–SW and the NW–SE sectors defined in Sect. 3.1. The sectors were divided in consecutive annular regions, centered at the nucleus, and selected to have ~ 1000 (background subtracted) counts in the spectra (inner-to-outer radii given in Tab. 4). The temperature and density of the innermost $2''$ radius region were derived using the last two ObsIDs (11269,12124) together, to avoid as much as possible contamination from the nucleus.

In addition to the sky background, it is necessary to account for the stellar contribution to the X-ray emission. We adopt the spectral model derived for M32 to account for the unresolved AB+CV emission (Boroson et al. 2011; Li, Z. et al. 2011), normalized by scaling it to the K-band light enclosed within the spectral extraction regions. The AB+CV model

is characterized by a combination of two thermal plasma emission components, with solar abundance and fixed temperatures of 0.4 keV and 4.6 keV, which are dominated by the emission of ABs and CVs, respectively (see Li, Z. et al. 2011 for details). An additional power law component, with a photon index of $\Gamma = 1.8$ and a normalization free to vary, is adopted to account for the residual contribution from low mass X-ray binaries (LMXBs; e.g., Kim et al. 2009). To account for PSF scattering of the nuclear emission, the best fit nuclear spectrum was included as a model component, with a scaling factor fixed to the PSF wing fraction (as determined from ChaRT and MARX simulations) in the spectral extraction region; this component is negligible ($\ll 1\%$) in all regions except the first annulus. We then characterize the diffuse gas by an APEC model component (with solar metal abundance).

Assuming a spherical geometry, we used the *project* model in XSPEC to perform a spectral deprojection. Before fitting, to account for the fact that only a fraction of the area is covered due to source removal, the ARFs generated for the annular regions were rescaled according to the missing area from source masking. The resulting best-fit spectral parameters are summarized in Tab. 4. The temperature is consistent with the 0.32 ± 0.02 keV value reported in Boroson et al. (2011) at the outer radii, but considerably hotter in the nuclear region and in the first annulus ($2''$ – $4''$), in all directions (Fig. 6). Without deprojection, this inner hot component with a similar temperature is found again at a significant level, thus it is not due to the *project* model.

Given the peculiar and unusual result of a significantly hotter thermal emission at the nucleus and in the surrounding $2''$ – $4''$ annulus, we next investigated whether the high temperature is a real feature of the hot gas, or could be due to an underestimate of the nuclear contribution. We focus on ObsID 11269 because of its depth and well characterized nuclear emission (pile-up free) in a single observation. We performed ChaRT+MARX simulations and found that the PSF wing may scatter 2% of the nuclear APEC component to the $2''$ – $4''$ radial bin (or a 0.5–2 keV flux of $6.0 \pm 1.2 \times 10^{-16}$ erg cm $^{-2}$ s $^{-1}$). The flux of the thermal component is 9×10^{-15} erg cm $^{-2}$ s $^{-1}$, which requires the PSF scattering fraction of the nuclear emission to be unrealistically underestimated (30% instead of 2%). Moreover, the contribution from unresolved stellar sources is an order of magnitude lower than the *APEC* component. Thus we conclude that the hot thermal component is significant, and arises from gas at a higher temperature in the inner \sim few hundreds pc.

The deprojected density in each spherical shell is shown in Fig. 7. Densities, along with other physical properties of interest for the hot gas, are presented in Tab. 5. We accounted for the fact that only a fraction of the area within a given annulus was covered, due to source removal. The electron number density n_e of the hot gas was derived from the emission measure ($\int n_e^2 dV$) of the APEC component given by the spectral fit of each extraction region.

A spherical geometry was assumed, and the volume covered by the quadrants was properly calculated using the apex angle of the two quadrants.

5. Summary of the observational results and discussion

A deep (579 ks) *Chandra* observation of the elliptical galaxy NGC4278, including two pointings during year 2010 and six pointings prior to 2010, has been analyzed with the following main results:

- The nuclear emission dominates the X-ray image, but its 0.5–8 keV flux in 2010 was the lowest among all pointings, and ~ 18 times lower than at its brightest state seen with *Chandra* (in 2005). At the nucleus, within $r = 2'' = 156$ pc, a power law spectral component (with $\Gamma = 2.31 \pm 0.20$, consistent with AGN emission) and a thermal component (with $kT = 0.75 \pm 0.05$ keV) coexist, respectively with an average $L_{0.5-8\text{keV}} = 2.5 \times 10^{39}$ erg s^{-1} during year 2010, and with $L_{0.5-8\text{keV}} = 1.0 \times 10^{39}$ erg s^{-1} .

- After merging data from all pointings, hot gas is detected out to a radius of ~ 5 kpc, with a total $L_{0.5-8\text{keV}} = 2.4 \times 10^{39}$ erg s^{-1} . On the galactic scale, the hot gas shows an elliptical shape, elongated in the NE-SW direction; its distribution is clearly different from that of the stellar component of the galaxy, having a flatter shape and a different orientation. The hot gas seems to follow the distribution of the ionized gas, that resides in a rotating, inner disk, and of the warm dust emission detected with *Spitzer*.

- The image ratio with the best-fit 2-D modeling of the surface brightness (i.e., the unsharp masking, Fig. 3) shows that the gas distribution surrounding the bright nucleus is not smooth, but includes regions where the brightness is lower than the average, and various clumps. In particular, two larger clumps are present NE and SW of the nucleus, at a distance of $\sim 10''$. These regions of enhancement of the brightness are not likely to be concentrations of stellar sources, being clearly extended; the spectral analysis of the diffuse emission also indicates thermal emission from hot gas, and not from fainter LMXBs.

- The 3D temperature and density profiles derived from deprojection along the NE-SW and NW-SE directions are consistent with each other at all radii, except for the temperature in the annulus surrounding the nucleus, that is lower in the direction of the elongation (NE-SW). The hot gas temperature stays at 0.6–0.8 keV out to a radius of ~ 300 pc, and drops sharply to ~ 0.3 keV outside, keeping a constant (or slowly decreasing) value out to ~ 5 kpc. The density profile shows a smooth decrease throughout the region examined.

The above results prompt the following questions: what is the origin of the nuclear

emission, and of the hotter gas at the galactic center? what produces the hot gas elongation? is there a relationship between the hot and the warm gas that seem to follow the same projected distribution? Taking also advantage of the radio information, we now investigate the hot gas origin and evolution, and the activity cycle, in this medium-mass elliptical galaxy; systems of this mass have not been investigated in detail previously. We examine in turn the origin of the nuclear emission in the next Sect. 5.1, that of the central hot gas in Sect. 5.2, and in Sect. 5.3 the relationship between the hot, warm, and cold gas phases.

5.1. The nuclear emission

The X-ray spectral shape of the low luminosity AGN during the most recent March 2010 pointings is consistent with that determined from pointings made between 2005 and 2007 by *Chandra*, and by *XMM-Newton* in 2004 (Tab. 2): during these previous brighter states, the average photon index was $\Gamma = 2.2_{-0.2}^{+0.1}$, affected by small intrinsic absorption ($N_H < 6.7 \times 10^{20} \text{ cm}^{-2}$; Younes et al. 2010). The source was brightest in 2004, and decreased by a factor of 5.7 by 2007; this trend of decrease in flux continued through 2010 (Sect. 4.1). Based on the spectral energy distribution from radio to X-rays, it was suggested that at low X-ray flux the nuclear emission is more typical of LINERs (and possibly originates in a RIAF and/or a jet), whereas at high X-ray flux it resembles more that of a Seyfert (Younes et al. 2010). The nucleus in 2010 had $L_{0.5-8 \text{ keV}}/L_{Edd} = 5.9 \times 10^{-8}$, where the Eddington luminosity $L_{Edd} = 4.25 \times 10^{46} \text{ erg s}^{-1}$ for the MBH mass in Tab. 1. The bolometric correction (L_{bol}/L_X) for low luminosity AGNs is believed to be lower than the value of standard AGNs (~ 30 , Elvis et al. 1994), where the accretion disk dominates the emission; for example, Ho (2009) suggested that $L_{bol}/L_{2-10 \text{ keV}} \approx 8$ for low luminosity AGNs, and, for a large sample including nuclei with $L_{bol}/L_{Edd} \lesssim 0.1$, a median $L_{bol}/L_{2-10 \text{ keV}} \approx 15.8$. Therefore the AGN in NGC4278 is a very sub-Eddington radiator (Tab. 3 gives the 2–10 keV nuclear luminosity), and its low luminosity could be the result of a low radiative efficiency, provided that the mass accretion rate is low. Thanks to the large dimming of the nucleus in 2010, we could derive the gas properties close to the MBH, a result used in what follows to derive an estimate of the mass accretion rate, and then to discuss the accretion modalities.

For material accreting on the MBH at rate \dot{M} , such that $\dot{m} = \dot{M}/\dot{M}_{Edd} \ll 0.01$ [where $\dot{M}_{Edd} = 22M_{BH}(10^9 M_\odot) M_\odot \text{ yr}^{-1}$], the accretion flow can become a RIAF, with an efficiency for producing radiation of $\epsilon \sim 10\dot{m}$ (Narayan & Yi 1995); the expected L_{bol} is then $\sim 10\dot{m}\dot{M}c^2$. We can adopt for \dot{M} the mass accretion rate given by the steady and spherically symmetrical Bondi (1952) solution, \dot{M}_B (e.g., Loewenstein et al. 2001, Di Matteo et al. 2003, Pellegrini 2005). An accretion rate $\lesssim \dot{M}_B$ enters also in the viscous

rotating analog of the Bondi treatment represented by the RIAF models (Quataert 2003, Narayan & Fabian 2011). \dot{M}_B is given by $\dot{M}_B = \pi G^2 M_{BH}^2 \frac{\rho_\infty}{c_{s,\infty}^3} \left[\frac{2}{5-3\gamma} \right]^{(5-3\gamma)/2(\gamma-1)}$, where γ is the polytropic index [$\gamma = 1$ (isothermal) to $5/3$ (adiabatic)], c_s is the sound speed, and “ ∞ ” refers to the ambient conditions (e.g., Frank et al. 2002). Ideally, one should insert in this formula the gas density and temperature at the accretion radius $r_{acc} = 2GM_{BH}/c_{s,\infty}^2$, where the dynamics of the gas start to be dominated by the potential of the MBH. In practice, one uses fiducial temperature and density for the circumnuclear region, determined as close as possible to the MBH. For the values for the nuclear region in Tabs. 4 and 5, one obtains $r_{acc} = 15 - 25$ pc, and $\dot{M}_B = (0.5 - 5) \times 10^{-3} M_\odot \text{ yr}^{-1}$ (for $\gamma = 5/3 - 1$); the corresponding $\dot{m}_B = (0.7 - 7) \times 10^{-4}$ is very low, within the RIAF regime. This \dot{M}_B is based on gas properties that are an average for a sphere of 156 pc radius ($\sim 6r_{acc}$), thus its value should be taken with some caution; for example, this \dot{M}_B may underestimate the true mass accretion rate at r_{acc} if the density rises steeply towards r_{acc} (but this seems not to be the case; see the modeling of Sect. 5.2.1).

Using an average $\gamma = 4/3$, then $\dot{M}_B = 2.1 \times 10^{-3} M_\odot \text{ yr}^{-1}$, and $L_{bol} = 10\dot{m}_B \dot{M}_B c^2 \sim 3.3 \times 10^{41} \text{ erg s}^{-1}$ (while a standard accretion disc would have a radiative output of $L_{acc} = 0.1\dot{M}_B c^2 \sim 1.2 \times 10^{43} \text{ erg s}^{-1}$); for the whole range of \dot{M}_B , $L_{bol} \sim (0.02 - 2) \times 10^{42} \text{ erg s}^{-1}$. Adopting a correction factor appropriate for the spectral energy distribution of a RIAF, i.e., $L_{0.5-8keV} \lesssim 0.15 L_{bol}$ (Mahadevan 1997), for the average $\dot{M}_B = 2.1 \times 10^{-3} M_\odot \text{ yr}^{-1}$ one expects $L_{0.5-8keV} \lesssim 5 \times 10^{40} \text{ erg s}^{-1}$, that is $\lesssim 20$ times larger than the observed $L_{0.5-8keV} = 2.5 \times 10^{39} \text{ erg s}^{-1}$ (the expected $L_{0.5-8keV} \lesssim 2.8 \times 10^{39} \text{ erg s}^{-1}$, for the lowest estimate of \dot{M}_B , and $\lesssim 3 \times 10^{41} \text{ erg s}^{-1}$ for the largest). Reductions of the mass accretion rate on the way to the MBH have often been claimed for RIAFs, since they include solutions where little of the mass available at large radii is accreted on the MBH due to outflows or convective motions (Blandford & Begelman 1999; Stone, Pringle, & Begelman 1999; Igumenshchev, Narayan, & Abramowicz 2003). Another source of reduction is given by the possibility that the gas has non-negligible angular momentum beyond the Bondi radius (Proga & Begelman 2003; Narayan & Fabian 2011). The latter authors calculated the rate at which mass accretes on to a MBH from rotating gas, for RIAFs in galactic nuclei, and found that $\dot{M} \sim (0.3 - 1)\dot{M}_B$, for a plausible viscosity parameter value ($\alpha = 0.1$). Large reductions of \dot{M} with respect to \dot{M}_B are not required here; for example, if $\dot{M} \sim 0.3\dot{M}_B$, accounting for only the effect of rotation, then L_{bol} would decrease by a factor of ~ 10 , and the predicted $L_{0.5-8keV}$ for the average \dot{M}_B would be $\lesssim 5 \times 10^{39} \text{ erg s}^{-1}$, close to that observed. The largest possible reduction in \dot{M}_B still reproducing the observed luminosity is of a factor of ~ 10 (calculated for the largest estimate of \dot{M}_B).

The accretion process at the nucleus of NGC4278 has also been studied recently by

modelling the radio-to-X-ray emission with an inner RIAF, an outer truncated thin accretion disk, and a jet, with the possibility of a radially varying mass accretion rate, within the RIAF region, to account for outflows (Nemmen et al. 2011). The radio was explained with a jet origin, the $100\mu\text{m}$ to $1\mu\text{m}$ emission required an outer accretion disk truncated at 30–100 Schwarzschild radii, and the X-rays could be equally well reproduced mostly by the RIAF (from inverse Compton scattering of synchrotron photons in the flow) or mostly by the jet (from synchrotron photons from the jet; see also Yuan & Cui 2005). The best fit models, respectively for the RIAF-dominated and the jet-dominated cases, have an accretion rate at the outer disk of⁷ $\dot{m}_{out} = 7$ or 4×10^{-4} , and an accretion rate on the MBH of $\dot{m}_{in} = 4.4$ or 0.9×10^{-4} . These \dot{m}_{out} values are within the \dot{m}_B range estimated here, and \dot{m}_{in} is not too different from \dot{m}_{out} ; for the case of the X-rays coming mostly from the RIAF, $\dot{m}_{out} = 1.6\dot{m}_{in}$, a result similar to what found above for the small reduction (if any) of \dot{m}_B to reproduce the observed $L_{0.5-8\text{keV}}$. In fact, the \dot{m}_B from our analysis, for $\gamma = 1.5$ as adopted by Nemmen et al., produces $L_{0.5-8\text{keV}} \lesssim 1.4 \times 10^{40} \text{ erg s}^{-1}$ if ending in a RIAF, and it should then be reduced by $\lesssim 2.3$ times to reproduce the observed luminosity.

In conclusion, the hot gas observed with *Chandra* near the MBH has density and temperature consistent with the idea that the nuclear luminosity comes from a RIAF, with a \dot{M} close to that estimated with the Bondi formula. If all the nuclear X-rays are to come from the accretion flow, \dot{M}_B can be reduced by a factor expected in case of rotation, still reproducing the observed luminosity; the latter constrains the reduction to be not larger than a factor of ~ 10 . If the X-rays come mostly from a nuclear jet, the accretion flow luminosity must be lower than that observed, and then a more important reduction for \dot{M}_B is allowed for, as can be achieved when outflows or convection are added. A further important constraint on how much mass must be accreting is given by the total energy output from accretion, as will be discussed in Sect. 5.2.3.

5.2. The origin of the central hotter gas

In a galaxy of the size of NGC4278, given standard assumptions concerning the type Ia supernova (SNIa) heating, the mass losses from evolving stars are expected to originate an outflow on the galactic scale (see also Sect. 5.2.1 below); this agrees with the low observed hot gas content, of a few $\times 10^7 M_\odot$ (Tab. 5). The intriguing central peak in temperature, instead, is a new finding, that could be produced by the following causes: 1) the MBH gravity field, 2) a nuclear outburst triggered by a past high accretion rate phase (i.e., in the

⁷ \dot{m} is the Eddington-scaled mass accretion rate.

AGN-mode), 3) hot accretion during a quiescent, low accretion rate state, 4) kinetic heating from the jet.

In the following, these hypotheses are examined in turn. The first one is studied with hydrodynamical simulations (Sect. 5.2.1); the next two are examined in light of the predictions of previous results from numerical simulations (Sect. 5.2.2); the last one is investigated through energetic calculations also exploiting the radio information (Sect. 5.2.3).

5.2.1. Hot gas evolution without AGN feedback

We performed hydrodynamical simulations for the evolution of the stellar mass losses, for a detailed galaxy model built for NGC4278, without feedback from the MBH; the aim is to establish what can and what cannot be explained by this basic model. The underlying 3-component galaxy mass model is made by the superposition of a stellar and a dark distributions, *plus a central MBH*, of mass fixed at that in Tab. 1. All other details regarding the galaxy model and the simulations are given in the Appendix.

The resulting gas flow on the galactic scale is an outflow driven by SNIa’s heating during the entire evolution; a small accretion region at the center is always present, due to the cuspy mass profile, typical of elliptical galaxies (e.g., Pellegrini 2012). With time increasing, the SNIa’s specific heating ($L_{SN}/\dot{M}_* \propto t^{0.2}$, where L_{SN} is the SNIa’s heating rate and \dot{M}_* is the stellar mass loss rate) slowly increases; this produces a decrease of the inflow velocity and of the radius of the inflowing region, that goes down to ~ 30 pc at the present epoch. At the center, the gas density keeps decreasing and the temperature increasing with time (Fig. 10 in the Appendix); mass flows through the innermost gridpoint (5 pc) at a decreasing rate, reaching $\dot{M} \sim 0.003M_\odot \text{ yr}^{-1}$ at the present epoch. Even though the density keeps rising towards the center in the model, this value of \dot{M} is within the range derived for \dot{M}_B in Sect. 5.1 (at its upper end).

The temperature and density profiles at an age consistent with that of the stellar population of NGC4278 (10.7 ± 2.14 , Terlevich & Forbes 2002) are shown in Fig. 8. Initially, the temperature drops towards the center, with a central value of ~ 0.55 keV at an age of ~ 10 Gyr; this value is an average calculated for a central sphere of radius of $2''$, as in the observations, and includes the contribution of a very inner region where the central MBH creates a spike in the gas injection temperature (see Fig. 8). Later, the central temperature becomes larger (~ 0.85 keV), and the temperature profile decreases smoothly out of $2''$ (Fig. 8, dotted line), without a sharp drop as instead observed. The model temperature is then larger than observed at the center, and agrees with that observed in the surrounding

annulus of radii $2'' - 4''$ only for the NW-SE quadrant; therefore, the observed temperature cannot be reproduced by the models as a long-lasting feature⁸. The model density profile is in reasonable agreement with the *Chandra* one at 10 Gyr, but it is lower than that, inwards of ~ 400 pc, for later epochs (Fig. 8). The MBH clearly heats the gas in its surroundings, through the combined effects of its gravitational field (causing gas compression) and of the increase in the stellar heating, due to the stellar velocity dispersion enhancement produced by the MBH within its sphere of influence⁹ (see the Appendix and its Fig. 9). This heating, though, keeps the gas temperature very high on a much smaller scale than observed (Fig. 8). Evidently, the gas properties close to the center are established by different (additional) phenomena, with respect to those simply connected with the MBH gravity, the SNIa’s heating, and mass input from stellar mass losses. This analysis also shows that accretion is possible even for gas with a central temperature as large as observed.

Another result of this investigation is that the observed temperature is lower than in the model, outwards of a ~ 0.5 kpc radius, and consistent just with the temperature expected from the thermalization of the stellar motions (T_σ ; Fig. 8). Note that the stellar heating could be lowered by at most $\sim 20\%$, for different mass models still consistent with the observational constraints. When coupled to the fact that also the model density tends to be lower than observed outside ~ 1 kpc, possibly indicating too much degassing, all this could point to a lower efficiency of the SNIa’s energy mixing process than standardly adopted. In fact the fraction of the SNIa’s kinetic energy that is turned into heat is uncertain, and may depend on the environment surrounding the expanding supernova remnants (e.g., Tang et al. 2009, Pellegrini 2011). In massive, hot gas-rich early type galaxies, SNIa’s bubbles should disrupt and share their energy with the local gas within $\sim 3 \times 10^6$ yr (Mathews 1990); in less massive spheroids in a global wind, instead, 3D hydrodynamical simulations of discrete SNIa’s heating suggest a non-uniform thermalization of the SNIa’s energy, with overheated gas advected outwards, carrying a large fraction of the SNIa energy with it (Tang et al. 2009). Another possibility is that the gas is cooled by the presence of other colder phases in the ISM (see Sect. 5.3).

⁸A temperature profile within ~ 400 pc similar to the observed one is produced between the two epochs shown in Fig. 8, but for a very brief time, lasting $\lesssim 10^7$ yr.

⁹The sphere of influence of the MBH has a radius of $r_{BH} = GM_{BH}/\sigma_0^2 = 23$ pc, for the M_{BH} and central σ values in Tab. 1.

5.2.2. Hot gas evolution with AGN-like outbursts

In the recent past NGC4278 could have experienced a nuclear outburst with a high \dot{m} , and the high central value of the gas temperature could be a remnant of that episode. Indeed, the inner $\sim 4''$ seem to contain a hot bubble, a region that appears to be overpressured with respect to its surroundings. Also, the absence of HI absorption against the nucleus (van Gorkom et al. 1989) suggests that the region around the center has been cleared of neutral gas; the *HST* WFPC2 images show that in the inner $\sim 2''$ diameter the dust lines are absent, and a pointlike bright nucleus is seen (Lauer et al. 2005). All this would be consistent with an inner region where the cooler gas has been removed, thus there is no dust and no HI absorption around the nucleus (consistent with the spectral results, Sect. 4.1). The effects of AGN feedback typical of accretion at high \dot{m} have been investigated in detail previously with spherically symmetric hydrodynamical simulations (Ciotti et al. 2010). During outbursts, very hot central gas is created (within ~ 100 pc), at a temperature that can reach up to a few keV; this central bubble is surrounded by gas at much lower temperature (kT drops down to 0.3–0.4 keV at ~ 1 kpc; Pellegrini et al. 2012), which resembles the observed trend in NGC4278. However, there are two caveats: the first is that the hot bubble lasts for a short time ($< 10^8$ yr), since it cools quickly and, soon after it is created, the accretion rate drops; furthermore, the outburst produces a low density region surrounding the nucleus, with an almost flat 0.3–2 keV brightness profile, extending to \sim a few kpc and lasting for $\sim 10^8$ yr (Pellegrini et al. 2012), and this large plateau in the brightness profile is not observed here (Fig. 2c). The second caveat is that high \dot{m} outbursts are coupled with starformation in the galactic central region, but NGC4278 shows a uniformly old stellar population, without signs of current or recent starformation (Shapiro et al. 2010, Kuntschner et al. 2010). All this supports the idea that nuclear outbursts at high \dot{m} are well confined in the past. In fact, an isolated galaxy of the mass of NGC4278 is expected to have a very small duty-cycle for the phases of accretion at high \dot{m} , over the past few Gyr, with the last bursting episode confined to a few Gyr ago (Ciotti & Ostriker 2012).

As these simulations with accretion at high \dot{m} show, after an outburst is terminated, a new sub-Eddington accretion phase establishes, where the nucleus is radiatively quiescent (\dot{m} is in the range of the RIAF regime). The galactic center, almost empty of gas, is replenished with the newly injected stellar mass losses, that feed the accreting flow and are kept hot by the MBH via compression, stellar heating, and the energy output from accretion. The gas behavior during this phase is similar to what is described in Sect. 5.2.1, and the temperature profile resembles that obtained without feedback at an epoch of 10.9 Gyr in Fig. 8 (Pellegrini et al. 2012); there is though less hot gas (at the same age). Therefore, even a post-outburst radiatively quiescent phase is not likely to explain the observed gas properties. The models considered in this Section include feedback expected from high \dot{m}

accretion, that is in radiative and mechanical form, with the latter from AGN winds only. At low $\dot{m} \ll 0.01$ the bulk of the accretion output is thought to be mostly mechanical, emerging in the form of jet/outflows rather than radiation (e.g., Merloni & Heinz 2008). Given the presence of a pc-scale jet in NGC4278, we examine in the next Sect. 5.2.3 whether a central hot region can be produced by mechanical heating. Note that the different temperature but the very similar density observed in the $2'' - 4''$ annulus, in the two NW-SE and NE-SW directions (Figs. 6 and 7), implies a variation in the thermal gas pressure from one quadrant to the next, at this fixed distance from the center: the pressure is larger perpendicular to the direction of the gas elongation (where the temperature is larger). The heating may have taken place along this preferential direction (the NW-SE one), that is also close to the jet directions (Fig. 4).

5.2.3. Jet heating (and confinement)

VLBA observations of the NGC4278 nucleus with a resolution of a few mas (~ 0.1 pc) at 5 and 8.4 GHz revealed synchrotron radio emission from a two-sided structure, made of two symmetric S-shaped jets emerging from a flat-spectrum core (Giroletti et al. 2005; see also Falcke et al. 2000). In total, the two-sided jet extends over ~ 45 mas, that is 3.5 pc. The distance reached by the currently observed jets is then smaller than the accretion radius ($r_{acc} \sim 15 - 25$ pc, Sect. 5.1), and much smaller than the size of the observed hot region (that extends out to $4''$, in the NW-SE direction).

The mildly relativistic velocity for the jet ($v_j/c \approx 0.76$) implies an epoch of jet ejection that is 10–100 yrs prior to the observation (Giroletti et al. 2005). These authors suggest that this source does not evolve into a kiloparsec scale radio galaxy, but rather ejects components that soon disrupt, without being able to travel long distances and form radio lobes. The lack of hot spots, that are instead prevalent in higher power compact symmetric objects (CSOs), indicates that the relatively low velocity jets may not be able to bore through the ISM and escape. The small size of the radio source was ascribed to a low-power central engine, which cannot create highly relativistic jets, possibly combined with the interaction with an interstellar medium. We address then the following questions: what is the energy flux for the jets? Is it likely that they are frustrated by the hot ISM in the nuclear region? Is it possible that (a fraction of) the jet energy has been deposited in this region, creating the hot central gas?

The average thermal pressure of the X-ray gas for the central $2''$ radius sphere is 5.8×10^{-10} dyn cm $^{-2}$ (Tab. 5), a value comparable to the pressure in the atmospheres of hot gas rich giant ellipticals, where the hot ISM often confines radio sources (e.g., Allen et al. 2006,

Cavagnolo et al. 2010). We can estimate the minimum pressure for the jets of NGC4278 from synchrotron theory, assuming energy equipartition between particles and magnetic field (e.g., O’Dea & Owen 1987). The spectral index of $a = -0.54$ ($S \propto \nu^a$) gives a good description of the emission over the whole radio band (VLA measurements are available from 74 MHz to 22 GHz), with a possible flattening below 408 MHz (Giroletti et al. 2005). Calculating a 74MHz–22GHz radio luminosity for the jets of 6.2×10^{38} erg s⁻¹, and assuming a volume emitting region for the jet that is a cylinder of height 45 mas and radius $r_j = 4$ mas, with filling factor $\phi = 1$, gives $p_{min} \sim 2 \times 10^{-6}$ dyn cm⁻². Then the jets can be thermally confined only if within few parsecs the thermal pressure becomes much larger than the average for the central 2'' (=156 pc). However, this p_{min} value is likely uncertain (e.g., due to the unknown source volume). An alternative way to estimate the jet internal pressure p_j is via the energy flux carried by a jet, that is via the jet power $P_{jet} \approx 4\pi r_j^2 v_j \gamma_j^2 p_j$, with γ_j the jet Lorentz factor (e.g., Owen, Eilek, & Kassim 2000). P_{jet} can be estimated from its relationship with the 5GHz radio core luminosity (Merloni & Heinz 2007); for an average $P_{5GHz} = 4.5 \times 10^{37}$ erg s⁻¹ for the core component resolved by the VLBA (Giroletti et al. 2005), the relation gives $P_{jet} = 2.5 \times 10^{42}$ erg s⁻¹. Cavagnolo et al. 2010 also presented relationships between the total synchrotron power, at 200–400 MHz, and the mechanical power of jets, measured from the cavity power. For a total $P_{200-400MHz} = 4.7 \times 10^{37}$ erg s⁻¹, then $P_{jet} = 1.1 \times 10^{42}$ erg s⁻¹. The jet power, again inferred from the cavities observed in the hot ISM of nearby radio ellipticals, correlates also with the accretion power $L_{acc} = 0.1 \dot{M}_B c^2$ (Allen et al. 2006). Inserting in this correlation the average $\dot{M}_B \sim 2.1 \times 10^{-3} M_\odot \text{ yr}^{-1}$ of Sect. 5.1, one finds $P_{jet} = 1.8 \times 10^{42}$ erg s⁻¹, in good agreement with the values given by the scalings with the radio luminosity. Note that these P_{jet} estimates imply a jet production efficiency $\epsilon_{jet} = P_{jet}/\dot{M}_B c^2 = 0.01 - 0.03$, that is P_{jet} is a significant fraction of L_{acc} . Unless P_{jet} is largely overestimated, mass needs then to be accreted at approximately the Bondi rate, derived for the gas properties close to the accretion radius; large reductions in the rate along the way to the MBH are not allowed (see also Allen et al. 2006). This completes the findings of Sect. 5.1 about the origin of the nuclear L_X , excluding the possibility that \dot{M}_B is reduced by orders of magnitude.

Adopting $P_{jet} \sim (1 - 2) \times 10^{42}$ erg s⁻¹, $\gamma_j = 1.5$ and $v_j = 0.76c$ (Giroletti et al. 2005), then $p_j \sim (1.6 - 3.3) \times 10^{-6}$ dyn cm⁻². To overcome this pressure, the hot ISM should become much hotter and denser within few pc from the MBH (the product nT should increase by a factor of $\gtrsim 10^3$ above the average within 2''). Whether this is indeed verified remains beyond testability with *Chandra*, but could be feasible, within a factor of few; for example, in a Bondi flow with $\gamma = 4/3$, the thermal pressure is $\propto r^{-2}$, and then can increase by a factor of $\sim 10^3$ moving inward by a factor of ~ 30 in radius; in a RIAF, the behavior of the pressure is similar (Narayan & Fabian 2011). Other cooler gas phases may contribute to the confinement of the jets, as cold gas (e.g., Emonts et al. 2010); however, there is no evidence

for them towards the nucleus, as discussed in Sect. 5.2.2. Alternatively, P_{jet} derived from the correlations above may be overestimated. If confinement is not feasible, the currently observed jets are really very young and just making their way through the hot ISM. Note, though, that extended radio emission out of the nucleus has not been detected, and that going down to the lowest frequency observed (~ 0.1 GHz), where “old” radio lobes should contribute if present producing an excess of emission, the radio spectrum does not steepen, but rather, if any, it flattens (e.g., Giroletti et al. 2005). From the relationship between a critical frequency above which the spectrum steepens due to ageing, that in this case is < 1 GHz, and the electron age, one derives that old, extended emission must date back to at least a few $\times 10^8$ yr (for a magnetic field of a few μG , as reasonable for an old radio lobe; e.g., Feretti & Giovannini 2008). Past radio activity seems then to have always been confined within the nuclear scale, or it took place more than a few $\times 10^8$ yr ago.

A jet could have heated the central gas via dissipation of the kinetic energy of shocks produced in the circumnuclear region. The heating by the jet of a region much larger than its currently observed extension requires that the activity phase started long before the estimated age (10-100 yr) for the component farthest from the nucleus. In fact, a plausible time to heat the gas is at least of the order of the sound crossing time t_s , and $t_s \sim 4 \times 10^5$ yr to cross the hot center out to $R = 2''$; $t_s \sim 10^6$ yr to reach $R = 4'' = 312$ pc. Heating of the center requires then at least $\sim 10^6$ yr. An upper limit to the time elapsed since the heating episode is given by the radiative gas cooling time for the center, that is $t_{cool} = 3kT/2n\Lambda(T, Z)$, where $\Lambda(T, Z)$ is the cooling function (taken here from Sazonov et al. 2005). For the innermost $2''$, $t_{cool} \sim 10^7$ yr, and t_{cool} is a factor of ~ 3 longer for the surrounding annulus. Then a radio outburst should have heated the gas not longer than $\sim 10^7$ yr ago. Indeed, in the hypothesis that this source is continuously ejecting components from the core that soon disrupt and cannot reach out of the nucleus, heating may be frequent, and confined to the galactic central region, keeping the gas hot there. The outburst duration in bright radio sources is quite well constrained to be $10^7 - 10^8$ yr (e.g., Worrall 2009); the outburst recurrence time, for radio sources with $L_{1.4\text{GHz}} > 10^{25}$ W Hz $^{-1}$, is such that each source is retriggered once every 0.5–few Gyr (Best et al. 2005, Worrall 2009). For lower luminosity sources, both the lifetimes and the recurrence times are more uncertain; it seems that the activity must be more frequently retriggered (Best et al. 2005). NGC4278 could then be an extreme case of frequent triggering of low power jet components¹⁰.

The final question is whether a past radio outburst could have injected enough heating

¹⁰Note that a hot accretion flow (as considered in Sects. 5.1 and 5.2.1) may well have resumed after a major heating episode of $\lesssim 10^7$ yr ago, since the flow time from $r_{acc} \sim 20$ pc to the center, at the free-fall velocity, is $\lesssim 10^5$ yr.

to produce at least the thermal energy of the central hot region currently observed, $E_{th} = 4.1 \times 10^{53}$ erg (within $2''$, Tab. 5). A jet power of the order of that estimated here, $P_{jet} \sim (1 - 2) \times 10^{42}$ erg s^{-1} , can account for E_{th} in $0.4-1 \times 10^4$ yr, a time much lower than typical lifetimes of individual radio sources (see above); clearly, this requires that the whole P_{jet} is transferred to the ISM. P_{jet} is also far larger than the gas luminosity within $2''$ (1.0×10^{39} erg s^{-1}) and within $4''$ (1.16×10^{39} erg s^{-1}).

5.2.4. Hot nuclei in other early type galaxies

In four other spheroids *Chandra* observations revealed a clear temperature increase towards the center. All these cases reside in low power radio galaxies ($L_{radio} < 2 \times 10^{38}$ erg s^{-1}), or where the radio emission is not detected at all. The first one was Sombrero (NGC4594, Pellegrini et al. 2003), where the LINER nucleus of $L(2 - 10 \text{ keV}) = 1.5 \times 10^{40}$ erg s^{-1} is embedded in 0.7 keV gas, out to $r \sim 160$ pc, and then surrounded by $kT \lesssim 0.4$ keV gas. This nucleus also hosts a compact radio source of low luminosity ($L_{15GHz} = 1.58 \times 10^{38}$ ergs s^{-1}). An increase in the central temperature was found in NGC 4649 (Humphrey et al. 2008), peaking at ~ 1.1 keV within the innermost 200 pc, and dropping to ~ 0.8 keV outside; NGC4649 is a faint radio source extending for ~ 4 kpc ($L_R = 1.4 \times 10^{37}$ erg s^{-1} , Dunn et al. 2010). The nuclear spectrum of the Virgo elliptical NGC4552 includes a power law from the AGN plus a thermal plasma with $kT = 1.04$ keV; 5GHz VLBA observations reveal a two-sided extended emission, suggestive of a pc-scale jetlike structure, of total radio luminosity of 1.55×10^{38} ergs s^{-1} (Machacek et al. 2006). Finally, a projected temperature of 0.65 keV within $2''$ and 0.40 keV within $2'' - 4''$ (for $d=9.7$ Mpc) was found in NGC3115 (Wong et al. 2011), with $L_X < 10^{38}$ erg s^{-1} and no detected radio emission; the central rise in temperature was attributed to the accretion flow.

A central temperature significantly larger than in the surroundings may be then a typical feature appearing during the activity cycle commonly followed by early type galaxies in the local universe. It could be the sign that sometimes, in the lifecycle of low power objects, the jet cannot bore out of the nucleus' surroundings, but it can heat them.

5.3. The extended, misaligned hot gas and the colder phases

One of the new and interesting findings from the deep observation of NGC4278 is the presence of hot gas, with a spatial distribution more elongated than the optical one, and also misaligned with it (Figs. 1 and 4). The soft diffuse X-ray emission seems instead aligned

with that of the ionized gas, residing in a rotating disk or spiral, of semi-major axis length of $\sim 25''$ (~ 2 kpc; Fig. 4; Sarzi et al. 2006; see also Osterbrock 1960, Goudfrooij et al. 1994). Thus there is a spatial association (in projection) between the hot and the ionized gas phases: both show an elongated distribution, following a direction described by the same position angle, and misaligned with respect to the optical major axis. The SAURON data show that the ionized gas velocity field is regular, consistent with circular gas motions in a low inclination disk, with a deviation from this simple situation in the outer measured region, due to a gradual twisting of the velocity field. The gas is rotating in the same sense as the stars, but with a kinematic misalignment, of a median angle of 29 ± 19 degrees within $22''$; the gaseous and stellar kinematics are misaligned by increasingly wider angles, towards the outer parts of the field (Sarzi et al. 2006). The ionized gas is not rotating in the equatorial plane of the galaxy, and its distribution and kinematics are likely tracing gas that is accumulating while flowing in (Sarzi et al. 2006). Finally, note that the SAURON angular resolution (each pixel is $\sim 1''$ wide) was adequate to establish that the ionized gas is diffuse and not filamentary (see also Goudfrooij et al. 1994).

NGC4278 also contains a large HI mass ($6.9 \times 10^8 M_\odot$, Sect. 1), residing in a large regular disk or ring (Raimond et al. 1981), extending for 37 kpc, which implies that the system is old and evolved; the tails from the disc, revealed by a deep map, indicate that the system is still accreting gas (Morganti et al. 2006). Notwithstanding the extensive reservoir of neutral hydrogen, and the very regular disc kinematics suggesting that the galaxy has been surrounded by cold gas for a few Gyr, there is no evidence for the presence of a young stellar population. Studies from various groups report a uniformly old age, from scales of $R_e/16$ to the whole galaxy (Terlevich & Forbes 2002, Serra et al. 2008, Jeong et al. 2009, Kuntschner et al. 2010, Shapiro et al. 2010). Therefore, rather than recent merging with starformation, smooth accretion from outside is suggested, with the gas spread over a large area, diluted and resulting in the formation of little CO emission and hence no star-formation (Morganti et al. 2006; CO emission is not detected, see Sect. 1, Crocker et al. 2011).

The HI disk extends down to the innermost resolution element of the Westerbork observation ($\approx 2 \times 1$ kpc), where the ionized gas resides; in the more central regions, the HI and the ionized gas are suggested to be physically associated, since they are spatially and kinematically consistent (Oosterloo et al. 2010, Morganti et al. 2006, Goudfrooij et al. 1994). Given this, and the fact that the radial profile of the $H\beta$ flux can be fully explained by photoionization by the LINER nucleus only within the central $3''$, but is clearly more extended than that, the ionised phase could be produced by shock-heating of the accreting gas (Sarzi et al. 2010; see also Eracleous et al. 2010b). A weak triaxial perturbation of the stellar potential could funnel the gas into preferential streams, where fast shocks between gas clouds may occur. A problem with this origin for the warm gas is that shock velocities

as high as required to power the observed line emission are not expected in the potential of NGC4278; other diffuse sources of ionization, as a hot ISM or old post-AGB stars, were then suggested to contribute or be dominant (Sarzi et al. 2010).

Finally, NGC4278 shows a complex and irregular dust structure in its core, with several dense knots, interconnected by filaments, and prominent patchy dust out to $\sim 25''$, mostly on the northern side of the nucleus; closer to the galactic center, due to a spiral pattern, the dust appears to be streaming toward the nucleus (Goudfrooij et al. 1994, Carollo et al. 1997, Lauer et al. 2005). *Spitzer* images revealed extended emission from warm dust, molecular hydrogen and ionized gas (see Fig. 4b), and IRS spectral observations shows excitation and ionization in the mid-IR (Tang et al. 2011).

Ionised gas, cold gas and dust then seem different phases of the same accretion process of gas from outside; moreover, the diffuse X-ray emission follows the general pattern of the [OIII] and $8\mu m$ emission, and thus is likely to be associated with the bar-like distribution of the other phases (Fig. 4). Is the hot gas interacting with these phases, and does its elongation find an explanation in this interaction? In fact, the flattening of the diffuse X-ray emission with respect to the optical surface brightness, and even more its misalignment, are an unexpected result: the hot gas originates in the stars, and at equilibrium its density should follow the isopotential surfaces, that are rounder than the optical isophotes, for reasonable galaxy models (e.g., Binney & Tremaine 1987). The origin of the hot gas elongation is not likely to reside in the presence of significant rotational support, inherited from the stars, from which the hot gas comes: in NGC4278 only the inner galactic region is occupied by a fast stellar rotator, with a maximum rotation of $\sim 70 \text{ km s}^{-1}$ at $0.4R_e$, and steeply decreasing outside. Also, the stellar kinematical axis is misaligned with respect to an axis perpendicular to the hot gas elongation (Fig. 4). Another potential contributing factor for the hot gas elongation could be an AGN outflow, if it cleared the ISM along directions perpendicular to the observed hot (and warm) gas elongation, in a sort of bipolar outflow (e.g., Novak et al. 2011). Since the ionized gas disk has a modest inclination, such an AGN outflow, while not ruled out, seems less likely; also, no significant kinematic disturbance is seen in the [OIII] SAURON velocity field, and then the elongated X-ray emitting region seems more a zone of enhanced emission. We also note that the same correlation between the X-ray emission, ionized gas, and $8\mu m$ emission in a flattened structure (Fig. 4) may be indicative of a dynamically supported ISM substructure (i.e., a gaseous bar, or warp, or some combination) located within the inner region of NGC4278. Even in this model the X-ray feature is not directly associated with the directionality of the AGN jets.

The energy flux from the hot to the cold gas, by increasing the X-ray emissivity, could be the reason why the hot gas seems not co-spatial with the stellar distribution, but instead

well aligned with the warm gas. The cold gas, accreting more or less steadily for a few Gyr, created within the galaxy a disk (or bar-like) region where the hot gas is made to cool preferentially, thus showing more emission there (e.g., Fabian et al. 2003). Thermal conduction is a specific example of an energy flux mechanism, and it has often been suggested to cause energy to flow from the hot coronal gas into colder gas, in elliptical galaxies and galaxy clusters (Sparks et al. 1989, Macchetto et al. 1996, Fabian et al. 2003). The ionized emission could result then from the cold accreting material that is being excited by the hot gas, during the evaporation process expected from the interaction between cold and hot gas. Thermal electron conduction excites the cold gas into optical emission, and locally enhances the X-ray emissivity and cools the hot gas; for example, two temperatures are present in the X-ray gas of M87, with the lower one in the vicinity of optical filaments (Sparks et al. 2004). Thus, electron conduction could explain, at least in part, also the discrepancy between the model and the observed temperatures out of few hundreds pc. We examine next the energetics involved more quantitatively.

Under the assumption that the energy flux is in the saturated regime (Cowie & McKee 1977), the energy available to excite the optical emission is $Q_{sat} = 5.2 \times 10^{40} T_7^{3/2} n_{0.01} D_{maj} D_{min}$, where $T_7 = T/10^7 \text{K}$ is the hot gas temperature, $n_{0.01} = n_e/0.01 \text{cm}^{-3}$ is its density, and $D_{maj} D_{min}$ is proportional to the apparent projected surface area (D_{maj} and D_{min} being the major and minor diameter of the line emitting region in kpc; Macchetto et al. 1996). The $\text{H}\alpha$ emission line flux that is produced is $L \sim 10^{39} T_7^{3/2} n_{0.01} D_{maj} D_{min}$, if 1% of Q_{sat} is radiated in the $\text{H}\alpha$ line, and the total surface area is twice the apparent projected surface area (this is a conservative assumption, that applies to the observed ellipse shown in projection by the disk, whose depth along the line of sight, and thickness, remain unknown). The gas temperature and density outside the central $3''$ radius, where the LINER has been shown to fully account for the ionization (Sarzi et al. 2010, their Fig. 4), are $T_7 = 0.37$ (for $kT = 0.32$ keV), and $n_{0.01} = 1$; for $D_{maj} \sim 4$ kpc and $D_{min} \sim 2$ kpc (Fig. 4), one has $L \sim 10^{39} \text{ erg s}^{-1}$. The total $\text{H}\alpha$ luminosity observed is $9.1 \times 10^{39} \text{ erg s}^{-1}$ (rescaled for our adopted distance), and $5.8 \times 10^{39} \text{ erg s}^{-1}$ of this comes from outside the central $3''$ radius (from data kindly provided by M. Sarzi). Thus the energy flux does not violate the limit given by the observed line emission, while contributing to the ionization of the extended warm gas distribution.

The presence of thermal conduction could also explain why the hot phase is colder than simple models predict, as shown by Fig. 8 (Sect. 5.2.1). The total energy flux from the hot gas to the cold one, Q_{sat} , turns out to be $\sim 10^{41} \text{ erg s}^{-1}$, a non-negligible amount. For example, the SNIa's heating for the whole galaxy amounts to $10^{41} \text{ erg s}^{-1}$ at an age of 10 Gyr. Indeed, remarkably, the hot gas temperature seems close to just the stellar heating prediction (Fig. 8), without traces of additional (e.g., from SNIa's) heat sources.

The timescale for this process of heat transfer from hot to cold gas (or the evaporation lifetime) is difficult to compute, because of the unknown internal density and distribution of the HI gas; however, given that the HI is much more massive than the hot gas, and still accreting, the process is not a fast, recent, and transient phenomenon (recall that also the hot gas is continuously replenished by stellar mass losses).

6. Conclusions

We analyzed a deep (579 ks) *Chandra* ACIS pointing of the radio compact elliptical galaxy NGC4278, hosting a two-sided pc-scale jet. We detected soft X-ray emission from hot gas out to a radius of ~ 5 kpc, with a 0.5–8 keV luminosity of 2.4×10^{39} erg s $^{-1}$, elongated and misaligned with respect to the stellar body. At the nucleus, AGN-like emission with a spectral shape consistent with that of previous pointings since 2004 ($\Gamma = 2.31 \pm 0.20$, and small intrinsic absorption) decreased by a factor of ~ 18 since the first *Chandra* observation. Hot gas is also present at the nucleus, with a temperature ($kT = 0.75$ keV) significantly larger than in the surrounding region, where $kT \sim 0.3$ keV. We investigated the relationships between nuclear emission, fuel availability, and mechanical energy output from accretion, as well as the interaction between hot and cold gas phases, with the following main results.

The low luminosity of the AGN [$L(0.5 - 8 \text{ keV})/L_{Edd} = 5.9 \times 10^{-8}$ in 2010] can be explained by a low radiative efficiency accretion flow, with mass accreting at a rate close to that of the Bondi accretion solution [$\dot{m}_B = (0.7 - 7) \times 10^{-4}$]. An average $\dot{M}_B = 2.1 \times 10^{-3} M_\odot \text{ yr}^{-1}$ corresponds to $L_{0.5-8\text{keV}} \lesssim 5 \times 10^{40}$ erg s $^{-1}$, while the observed $L_{0.5-8\text{keV}} = 2.5 \times 10^{39}$ erg s $^{-1}$; however, the effect of rotation in the gas close to the accretion radius can easily reduce this expected $L_{0.5-8\text{keV}}$ to $\lesssim 5 \times 10^{39}$ erg s $^{-1}$. Estimates of the jet power from scalings with the radio luminosity at 5 GHz and 200–400 MHz, and with \dot{M}_B , all agree giving $P_{jet} = (1 - 2) \times 10^{42}$ erg s $^{-1}$. This power requires that the rate of accretion \dot{M} on the MBH is not largely reduced with respect to \dot{M}_B .

The hot gas flow, followed with hydrodynamical simulations including heating by SNIa's and only gravitational effects from the MBH, is an outflow on the galactic scale during the entire evolution, consistent with the low observed hot gas content. There is also a small accretion region at the center, through which mass flows on the MBH at a rate consistent with the estimate of \dot{M}_B , at the present epoch. The MBH heats the surrounding gas on a much smaller region than observed, and the large and sharp temperature increase at the center is not reproduced; also, out of the central ~ 0.5 kpc the model temperature is larger than observed, indicating that the SNIa's heating is less important than standardly assumed, or that the gas is cooling due to the interaction with other gas phases. An MBH outburst

in the recent past due to accretion at high \dot{m} would be supported by the finding of a central overpressured region in the hot gas, and of a central “hole” in the cooler gas phases; however, it is not likely to be the origin of the central large temperature, since it should have also left a flatter brightness profile than observed in the central galactic region, and traces of starformation.

A jet could have heated the central gas, during a past activity episode, taking place a time $\lesssim t_{cool} \sim 10^7$ yr ago. Extended radio emission is not detected, and the radio spectrum does not show signs of older lobes, thus it is likely that also in the past radio outbursts have not succeeded in getting out of the central galactic region. The central temperature may then have originated by a frequent triggering of low power jet components, that remain confined within the nucleus. A high temperature at the center may be a typical feature appearing during the activity cycle of low power objects, when the jet cannot bore out of the nucleus surroundings, but it can heat them. Unless P_{jet} has been overestimated, the thermal confinement of the pc-scale jets requires the hot gas pressure to increase by a large factor ($\gtrsim 10^3$) above its average over the central 156 pc. Other colder gas phases seem to have been cleared from the nuclear region.

On the galactic scale, there is a spatial association (in projection) between the hot, the cold and the ionized gas phases, both elongated in the same direction, misaligned with respect to the optical major axis. The accreting cold gas triggering the cooling of the hot phase could produce both the unusual elongation and misalignment of the X-ray emission, and the lower temperature of the hot gas with respect to the predictions of hydrodynamical simulations. Part of the ionized emission could result from the cold gas excited by the hot gas, during the evaporation process.

Investigations of the interplay between the hot gas and the nuclear activity are fundamental in the context of understanding the MBH-host galaxy coevolution; NGC4278 is the first case of a low/medium mass galaxy, with a modest hot gas content, that has been explored in detail using *Chandra* observations. Even though expensive in terms of exposure time, other studies of similar objects are very much needed to build a coherent and comprehensive picture of accretion in the local universe. The interplay between different gas phases, as resulting from multiwavelength observations, is another field rich of consequences for our knowledge of the galactic ecology and evolution, and allowed here for a more exhaustive explanation of the hot gas properties as well.

We thank L. Ciotti, G. Giovannini and R. Sancisi for useful discussions, and M. Sarzi for kindly providing data and the ionized gas images used for Fig. 4. This work was partially supported by the Chandra GO grant GO0-11102X (PI: Fabbiano) and NASA contract NAS8-

39073 (CXC). GT and SP also acknowledge partial financial support from the ASI-INAF grant I/009/10/0. The data analysis was supported by the CXC CIAO software and CALDB. We have used the NASA NED and ADS facilities, and have extracted archival data from the Chandra archives. *Facility*: CXO (ACIS).

REFERENCES

- Allen, S.W., Dunn, R.J.H., Fabian, A.C., Taylor, G.B., Reynolds, C.S. 2006, MNRAS 372, 21
- Anders, E., & Grevesse, N. 1989, *Geochim. Cosmochim. Acta*, 53, 197
- Bertola, F., Pizzella, A., Persic, M., Salucci, P. 1993, ApJ 416, L45
- Best, P. N., Kauffmann, G., Heckman, T. M., Brinchmann, J., Charlot, S., Ivezić, Z., White, S. D. M. 2005, MNRAS 362, 25
- Binney, J., Tremaine, S. 1987, *Galactic dynamics*, Princeton University Press
- Bîrzan, L., McNamara, B. R., Nulsen, P. E. J., Carilli, C. L., Wise, M. W. 2008, ApJ 686, 859
- Blandford, R. D., Begelman, M. C. 1999, MNRAS 303, L1
- Bondi, H. 1952, MNRAS, 112, 195
- Boroson, B., Kim, D.-W., Fabbiano, G. 2011, ApJ 729, 12
- Brassington, N. J., Fabbiano, G., Kim, D.-W., et al. 2009, ApJS 181, 605
- Cappellari, M., Bacon, R., Bureau, M., et al. 2006, MNRAS, 366, 1126
- Cappellari, M., Emsellem, E., Bacon, R., et al. 2007, MNRAS 379, 418
- Cappellaro, E., Evans, R., Turatto, M., 1999, A&A, 351, 459
- Carollo, C. M., Danziger, I. J., Rich, R. M., Chen, X. 1997, ApJ 491, 545
- Cattaneo, A., Faber, S. M., Binney, J., et al. 2009, Nature 460, 213
- Cavagnolo, K. W., McNamara, B. R., Nulsen, P. E. J., Carilli, C. L., Jones, C., Bîrzan, L. 2010, ApJ 720, 1066
- Ciotti, L., Ostriker, J. P., Proga, D. 2010, ApJ 717, 708

- Ciotti, L., Ostriker, J. P., 2012, in *Hot Interstellar Matter in Elliptical Galaxies*, Astrophysics and Space Science Library, Vol. 378, p. 83. Springer. (arXiv:1104.2238)
- Cohen, A. S., Röttgering, H. J. A., Jarvis, M. J., Kassim, N. E., Lazio, T. J. W. 2004, ApJS 150, 417
- Cowie, L. L., McKee, C. F. 1977, ApJ 211, 135
- Crocker, A. F., Bureau, M., Young, L. M., Combes, F. 2011, MNRAS 410, 1197
- David, L.P., et al. 2009, ApJ 705, 624
- Davis, J. E. 2001, ApJ 562, 575
- Diehl, S., Statler, T. S. 2008, ApJ 680, 897
- Di Matteo, T., Springel, V., Hernquist, L. 2005, Nature 433, 604
- Di Matteo, T., Allen, S. A., Fabian, A.C., Wilson, A.S., Young, A.J. 2003, ApJ 582, 133
- Doe, S., Nguyen, D., Stawarz, C., et al. 2007, ASPC 376, 543
- Dunn, R. J. H., Allen, S. W., Taylor, G. B., Shurkin, K. F., Gentile, G., Fabian, A. C., Reynolds, C. S. 2010, MNRAS 404, 180
- Elvis, M., Wilkes, B. J., McDowell, J., et al. 1994, ApJS 95, 1
- Emonts, B. H. C., Morganti, R., Struve, C., et al. 2010, MNRAS 406, 987
- Eracleous, M., Hwang, J.A., Flohic, Hélène M. L. G. 2010a, ApJS, 187, 135
- Eracleous, M., Hwang, J.A., Flohic, Hélène M. L. G. 2010b, ApJ, 711, 796
- Fabbiano, G., Brassington, N. J., Lentati, L., et al. 2010, ApJ 725, 1824
- Fabian, A.C., Sanders, J.S., Crawford, C.S., Conselice, C.J., Gallagher, J.S., Wyse R.F.G. 2003, MNRAS 344, L48
- Falcke, H., Nagar, N. M., Wilson, A. S., Ulvestad, J. S. 2000, ApJ 542, 197
- Feretti, L., Giovannini, G. 2008, LNP 740, 143
- Forman, W., Jones, C., Churazov, E., et al. 2007, ApJ, 665, 1057
- Freeman, P. E., Kashyap, V., Rosner, R., & Lamb, D. Q. 2002, ApJS, 138, 185

- Frank, J., King, A., Raine, D.J., 2002, *Accretion Power in Astrophysics*, Cambridge University Press
- Gallo, E., Treu, T., Marshall, P.J., Woo, J.-H., Leipski, C., Antonucci, R. 2010, ApJ 714, 25
- Garcia, A.M. 1993, A&A Suppl. Ser. 100, 47
- Garmire, G. P., Bautz, M. W., Ford, P. G., Nousek, J. A., & Ricker, Jr., G. R. 2003, Proc. SPIE, 4851, 28
- Giroletti, M., Taylor, G. B., Giovannini, G. 2005, ApJ 622, 178
- Goudfrooij, P., Hansen, L., Jorgensen, H. E., & Norgaard-Nielsen, H. U. 1994, A&AS, 105, 341
- Haardt, F., Maraschi, L. 1993, ApJ 413, 507
- Ho, L.C., Filippenko, A. V., & Sargent, W.L. W. 1997, ApJ 487, 568
- Ho, L.C. 2008, ARAA 46, 475
- Ho, L.C. 2009, ApJ 699, 626
- Hopkins, P.F., Hernquist, L., Cox, T.J., Roberston, B., Di Matteo, T., Springel, V., 2005, ApJ, 625, L71
- Humphrey, P. J., Buote, D.A., Brighenti, F., Gebhardt, K., Mathews, W. G. 2008, ApJ 683, 161
- Jarrett, T. H., Chester, T., Cutri, R., Schneider, S. E., Huchra, J. P. 2003, AJ 125, 525
- Jeong, H., Yi, S. K., Bureau, M., et al. 2009, MNRAS 398, 2028
- Johansson, P.H., Naab, T., Burkert, A., 2009, ApJ, 690, 802
- Kaviraj, S., Schawinski, K., Silk, J., Shabala, S.S. 2011, MNRAS 415, 3798
- Kim, D.-W., Fabbiano, G., Brassington, N. J., et al. 2009, ApJ 703, 829
- Kronawitter, A., Saglia, R. P., Gerhard, O., Bender, R. 2000, A&AS 144, 53
- Kuntschner, H., Emsellem, E., Bacon, R., et al. 2010, MNRAS 408, 97
- Lauer, T.R., Faber, S. M., Gebhardt, K., et al. 2005, AJ 129, 2138
- Li, W., et al. 2011, MNRAS, 412, 1473

- Li, Z., Jones, C., Forman, W. R., et al. 2011, *ApJ*, 730, 84
- Loewenstein, M., Mushotzky, R.F., Angelini, L., Arnaud, K.A., & Quataert, E. 2001, *ApJ* 555, L21
- Macchetto, F., Pastoriza, M., Caon, N., Sparks, W. B., Giavalisco, M., Bender, R., Capaccioli, M. 1996, *A&AS* 120, 463
- Machacek, M., Nulsen, P. E. J., Jones, C., Forman, W. R. 2006, *ApJ* 648, 947
- Mahadevan, R. 1997, *ApJ* 477, 585
- Maoz, D. 2007, 377, 1696
- Maoz, D., Mannucci, F., Li, W., Filippenko, A. V., Della Valle, M., & Panagia, N. 2011, *MNRAS*, 412, 1508
- Maraston, C. 2005, *MNRAS* 362, 799
- Mathews, W.G., 1990, *ApJ* 354, 468
- Merloni, A., Heinz, S., 2007, *MNRAS* 381, 589
- Merloni, A., Heinz, S., 2008, *MNRAS* 388, 1011
- Million, E.T., Werner, N., Simionescu, A., et al., 2010, *MNRAS* 407, 2046
- Morganti, R., de Zeeuw, P. T., Oosterloo, T. A., et al. 2006, *MNRAS* 371, 157
- Nagar, N. M., Wilson, A. S., Falcke, H. 2001, *ApJ* 559, L87
- Narayan, R., Yi, I. 1995, *ApJ* 452, 710
- Narayan, R., Fabian, A. C. 2011, *MNRAS* 415, 3721
- Navarro, J.F., Frenk, C. S., White, S. D. M. 1997, *ApJ* 490, 493
- Nemmen, R., Storchi-Bergmann, T., Eracleous, M. 2011, submitted to *ApJ* (arXiv:1112.4640)
- Novak, G. S., Ostriker, J. P., Ciotti, L. 2011, *ApJ* 737, 26
- O’Dea, C. P., Owen, F. N. 1987, *ApJ* 316, 95
- Oosterloo, T., Morganti, R., Crocker, A., et al. 2010, *MNRAS* 409, 500

- Osterbrock, D. E. 1960, ApJ, 132, 325
- Owen, F.N., Eilek, J.A., Kassim, N. E. 2000, ApJ 543, 611
- Pellegrini, S., Baldi, A., Fabbiano, G., Kim, D.-W. 2003, ApJ 597, 175
- Pellegrini, S., 2005, ApJ 624, 155
- Pellegrini, S., 2010, ApJ 717, 640
- Pellegrini, S. 2011, ApJ 738, 57
- Pellegrini, S., Ciotti, L., Ostriker, J.P. 2012, ApJ 744, 21
- Pellegrini, S., 2012, in *Hot Interstellar Matter in Elliptical Galaxies*, Astrophysics and Space Science Library, Vol. 378, p. 21. Springer. (arXiv:1112.2140)
- Proga, D., Begelman, M. C. 2003, ApJ 592, 767
- Ptak, A. Terashima, Y., Ho, L.C., Quataert, E. 2004, ApJ 606, 173
- Quataert, E. 2003, ANS 324, 435
- Raimond, E., Faber, S. M., Gallagher, J. S., III, & Knapp, G. R. 1981, ApJ, 246, 708
- Sarzi, M., Shields, J. C., Schawinski, K., et al. 2010, MNRAS 402, 2187
- Sarzi, M., Falcón-Barroso, J., Davies, R., et al. 2006, MNRAS 366, 1151
- Sazonov, S. Yu., Ostriker, J. P., Ciotti, L., Sunyaev, R. A. 2005, MNRAS 358, 168
- Schawinski, K., Lintott, C. J., Thomas, D., et al. 2009, ApJ 690, 1672
- Schilizzi, R. T., Fanti, C., Fanti, R., Parma, P. 1983, A&A 126, 412
- Serra, P., Trager, S. C., Oosterloo, T. A., Morganti, R. 2008, A&A 483, 57
- Shapiro, K. L., Falcón-Barroso, J., van de Ven, G. et al. 2010, MNRAS 402, 2140
- Silk, J., Rees, M. J. 1998, A&A 331, L1
- Sparks, W. B., Macchetto, F., Golombek, D. 1989, ApJ 345, 153
- Sparks, W. B., Donahue, M., Jordan, A., Ferrarese, L., Côté, P. 2004, ApJ 607, 294
- Tang, S., Wang, Q. D., Mac Low, M., Joung, M. R. 2009, MNRAS 398, 1468

- Tang, Y., Gu, Q., Zhang, S., Tang, B. 2011, MNRAS 414, 1827
- Terashima, Y., & Wilson, A. S. 2003, ApJ 583, 145
- Terlevich, A. I., Forbes, D. A. 2002, MNRAS 330, 547
- Tonry, J.L., Dressler, A., Blakeslee, J.P., et al. 2001, ApJ 546, 681
- Tremaine, S., Gebhardt, K., Bender, R., et al. 2002, ApJ 574, 740
- van Gorkom, J. H., Knapp, G. R., Ekers, R. D., Ekers, D. D., Laing, R. A., Polk, K. S. 1989, AJ 97, 708
- Wong, K.-W., Irwin, J., Yukita, M., Million, E., Mathews, W., Bregman, J.N. 2011, ApJ 736, L23
- Worrall, D. M. 2009, A&ARv 17, 1
- Wrobel, J. M., Heeschen, D. S. 1984, ApJ 287, 41
- Younes, G., Porquet, D., Sabra, B., Grosso, N., Reeves, J. N., Allen, M. G. 2010, A&A 517, 33
- Yuan, F., Cui, W. 2005, ApJ 629, 408

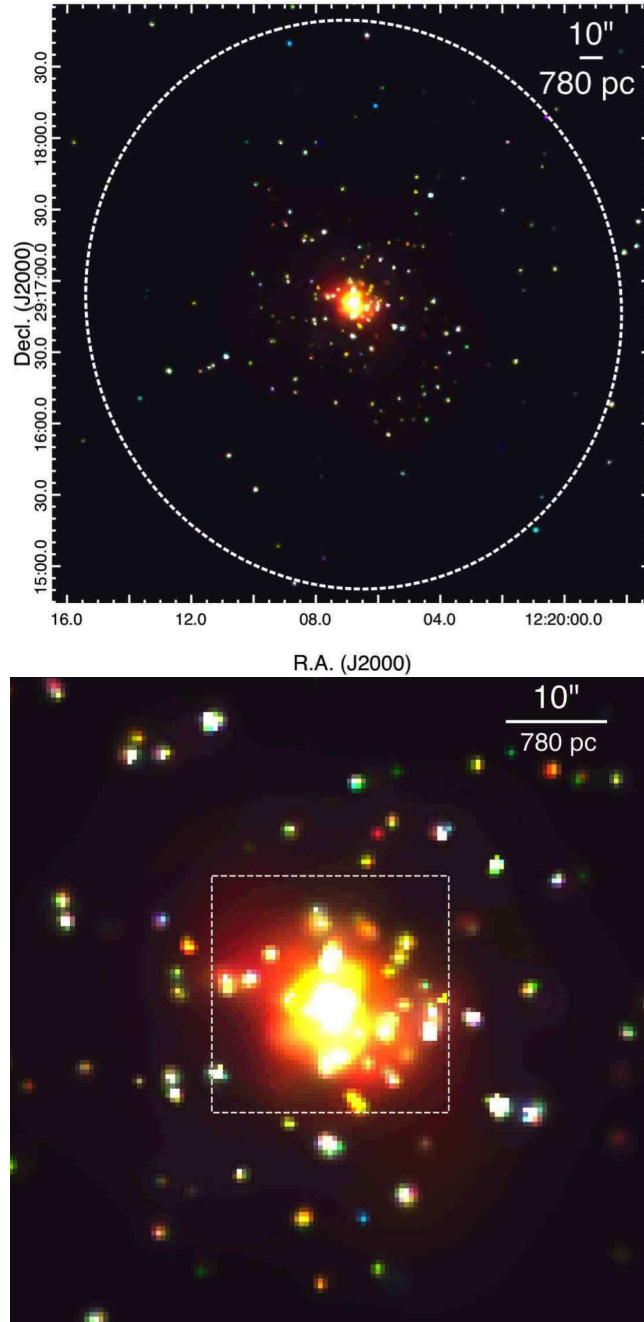


Fig. 1.— Top (a): three-color composite image ($4' \times 4'$) of NGC 4278. Red represents the 0.3-0.9 keV X-ray emission, green represents the 0.9–2.5 keV emission, and blue the 2.5–8 keV emission. North is up, East is to the left. The white dashed ellipse indicates the extent and orientation of the optical D25 ellipse. Bottom (b): the zoomed-in X-ray image of the central $70''$ region; the dashed square shows the region zoomed in the next Fig. 1c. See Sect. 2 and 3.1 for more details.

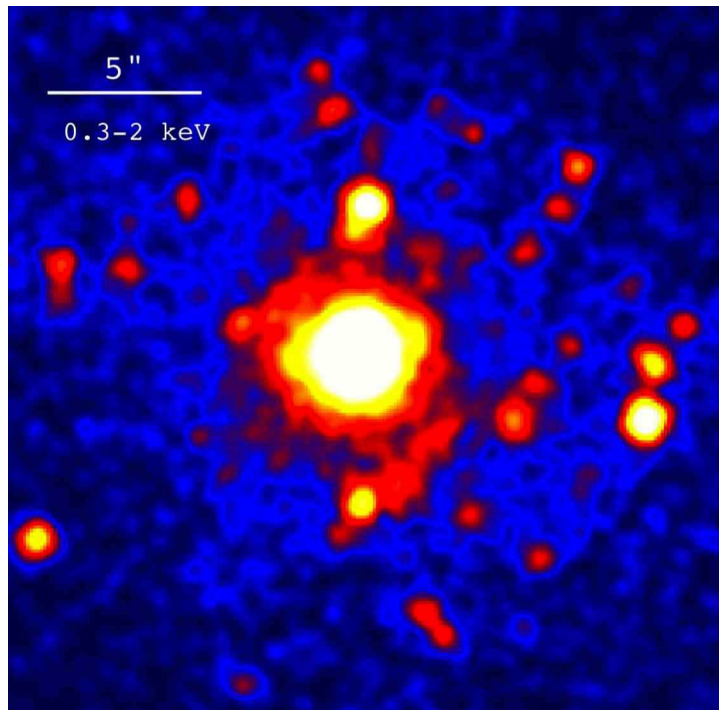


Fig. 1.— Continued. (c) The innermost $20''$ region showing the subpixel rebinned X-ray emission (0.3–2 keV; smoothed with a $FWHM = 0.3''$ gaussian kernel). See Sect. 3.1 for more details.

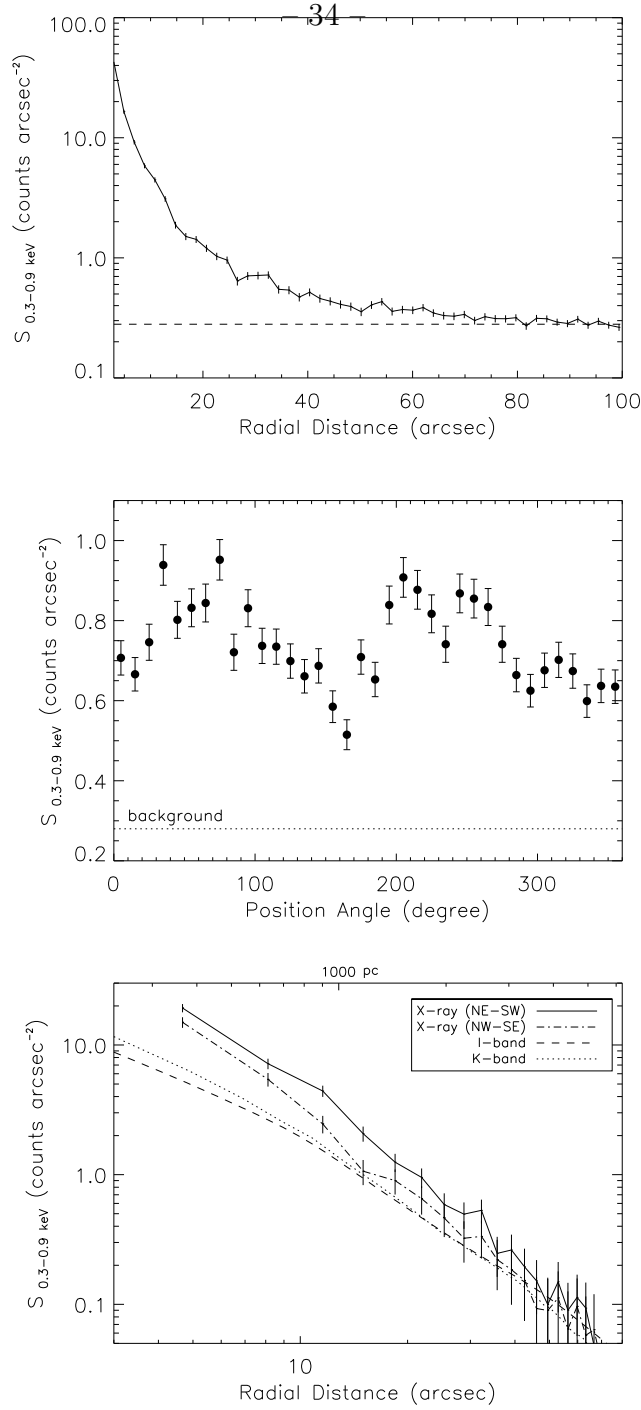


Fig. 2.— Top: (a) azimuthally averaged radial profile of the diffuse X-ray emission (point sources masked) in the 0.3–0.9 keV band. Middle (b): average surface brightness for the extended soft X-ray emission, measured in 36 “fan-shape” sectors, each 10° wide, starting from N and moving towards E, and each one extending from a radius of $2''$ (thus excluding the nucleus) out to $60''$. Bottom (c): background subtracted, azimuthally averaged radial profiles in the NE-SW and the NW-SE sectors. The dashed and dotted lines are the radial profiles in the optical I-band (Cappellari et al. 2006) and the near-IR K band (Jarrett et al. 2003). See Sect. 3.1 for more details.

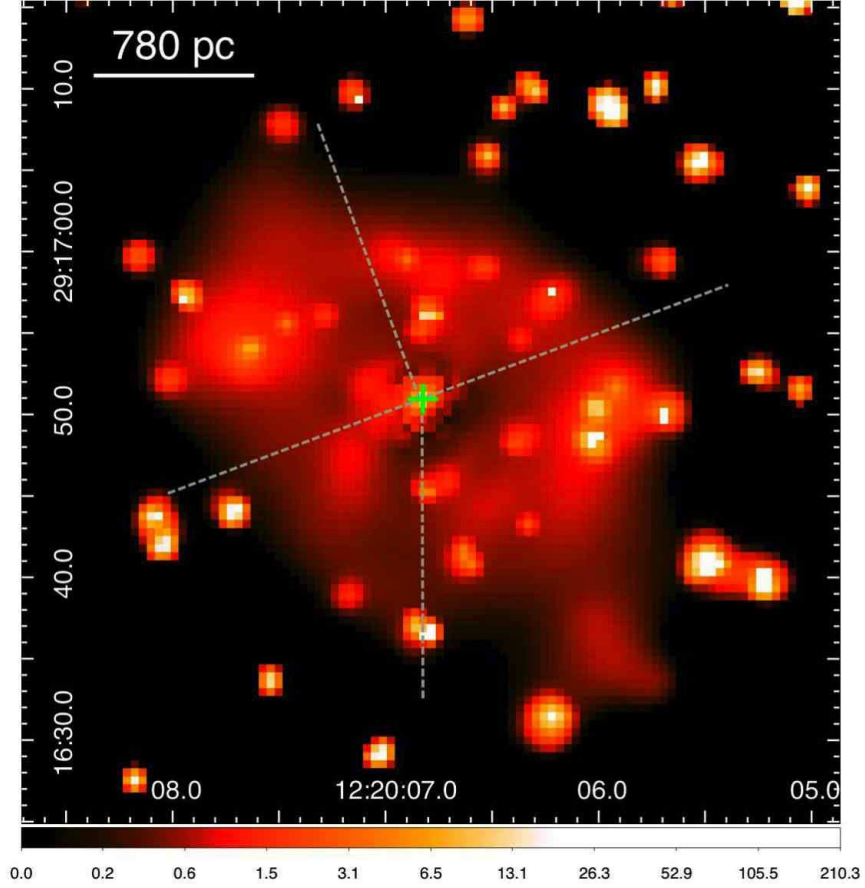


Fig. 3.— The intensity ratio image between the background subtracted soft X-ray emission and the 2-D *beta* model image. The soft X-ray image was adaptively smoothed with a minimum significance of 2.5σ . The four grey lines indicate the boundaries of the quadrants defined in Section 3.1. The optical center is shown with the green cross, and the 780 pc bar (top left) is equivalent to $10''$. See Sect. 3.1 for more details.

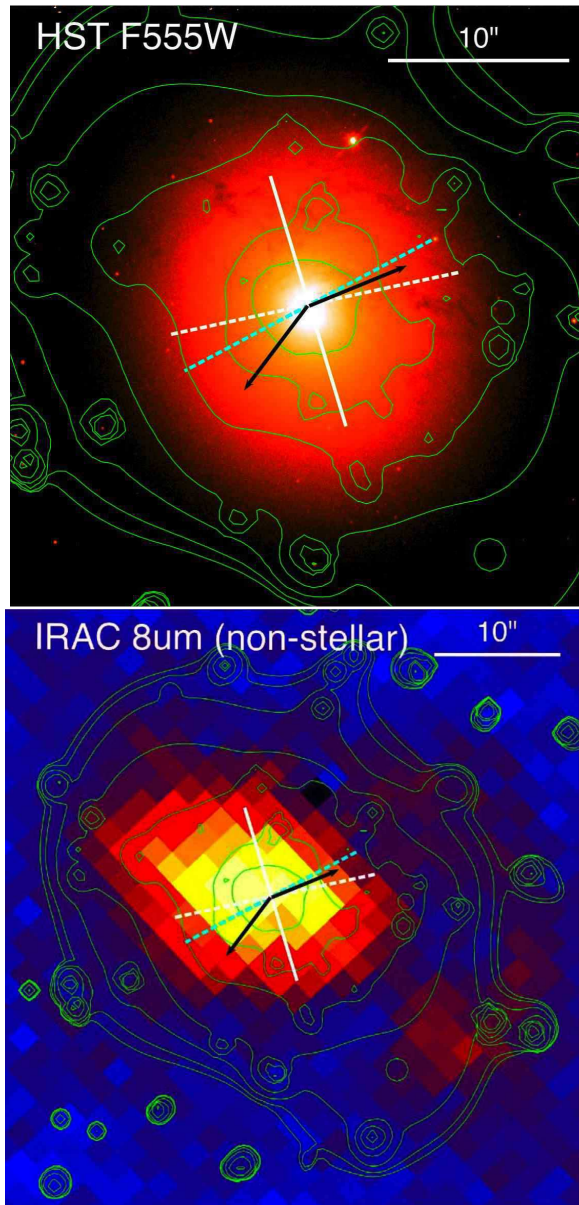


Fig. 4.— Contours of the extended X-ray emission in the 0.3–0.9 keV band overlaid on: top (a) the *HST* WFPC2 V band image (Carollo et al. 1997); bottom (b) the *Spitzer* IRAC 8 μ m emission (with stellar continuum removed; see Tang et al. 2011). Note that the *HST* image has a smaller field of view. Relevant position angles are shown: the current radio jet directions (black arrows, from the knots S1 and N2 in the high resolution radio map of Giroletti et al. 2005); the major axis of the optical light distribution in the inner galactic region ($PA_{phot}=16.7^\circ$, Cappellari et al. 2007; white solid line), and the rotation axis of the stars in the inner galactic region (a line perpendicular to the kinematic $PA_{kin}=12.0^\circ$, Cappellari et al. 2007; white dashed line); the rotation axis for the ionized gas (Sarzi et al. 2006; cyan dashed line). See Sect. 3.2 for more details.

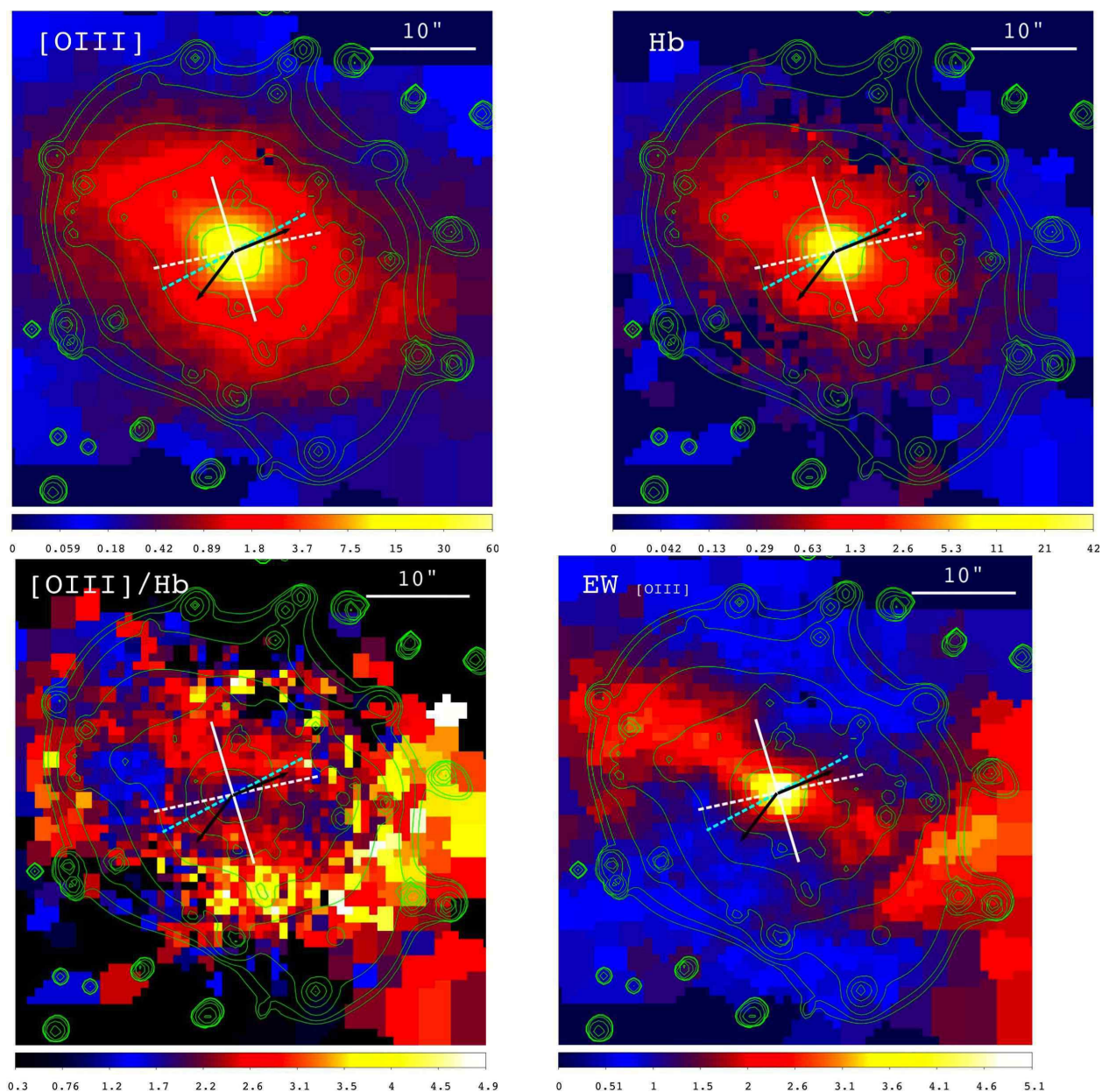


Fig. 4.— Continued. (c) Contours of the extended X-ray emission in the 0.3–0.9 keV band overlaid on the ionized gas maps from the SAURON survey (Sarzi et al. 2006); top left: [OIII] flux; top right: H β flux; bottom left: [OIII]/H β ; bottom right: EW_[OIII]. The hot gas is elongated in a direction more aligned with the ionized gas distribution and the *Spitzer* IRAC 8 μ m emission than with the optical stellar body of the galaxy. See Sect. 3.2 for more details.

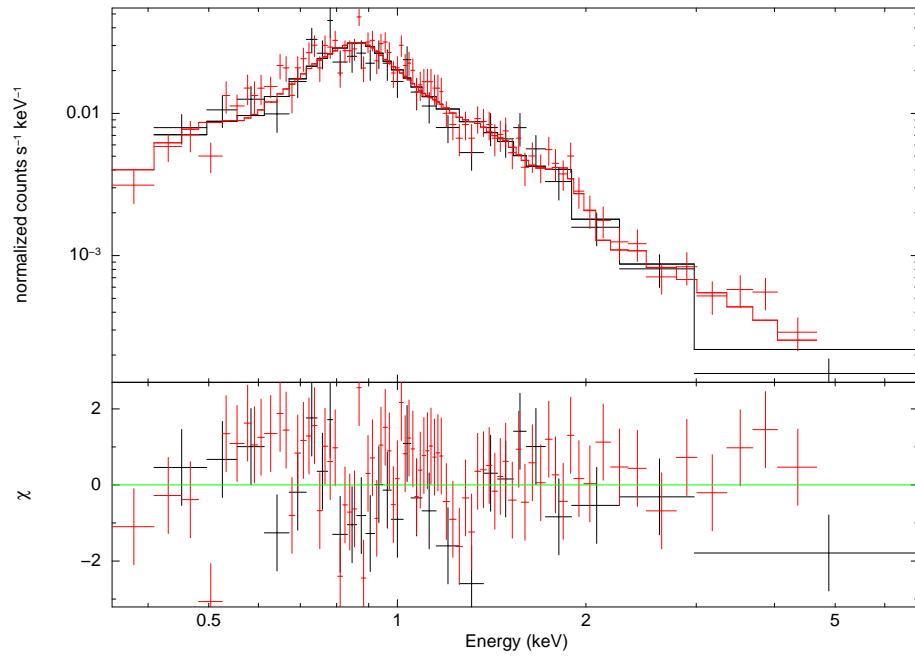


Fig. 5.— Best fit spectrum of the nuclear emission using the last two observations of March 2010 (Tab. 2) that are not affected by pile-up. The red and black lines correspond to the nuclear spectra from ObsID 11269 and 12124, respectively. See Sect. 4.1 for more details.

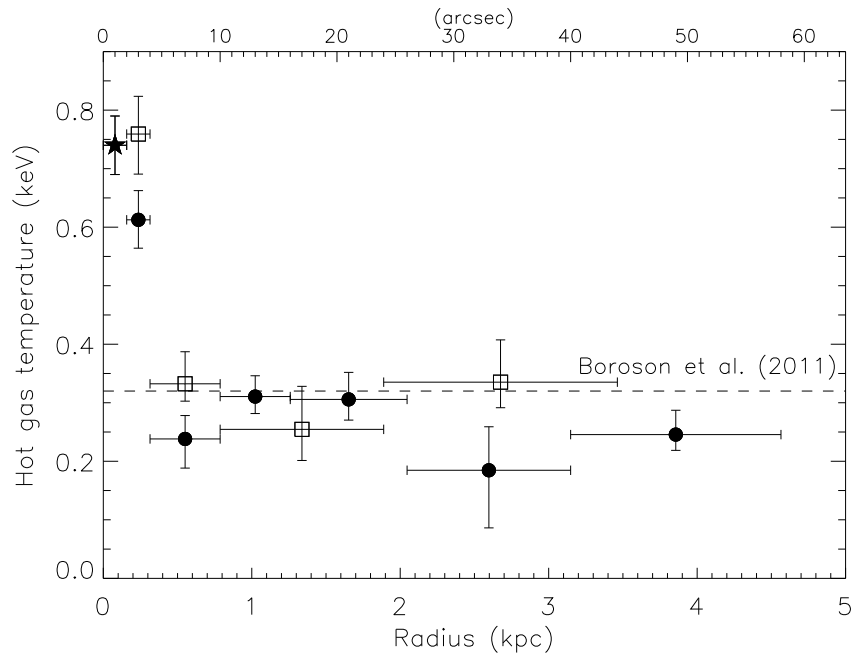


Fig. 6.— Radial distribution of gas temperature derived from spectral deprojection along two directions (NE–SW, filled circles; and NW–SE, open boxes). The temperature for the inner $2''$ derived using only the last two observations is shown as a star. See Sect. 4.2 for more details.

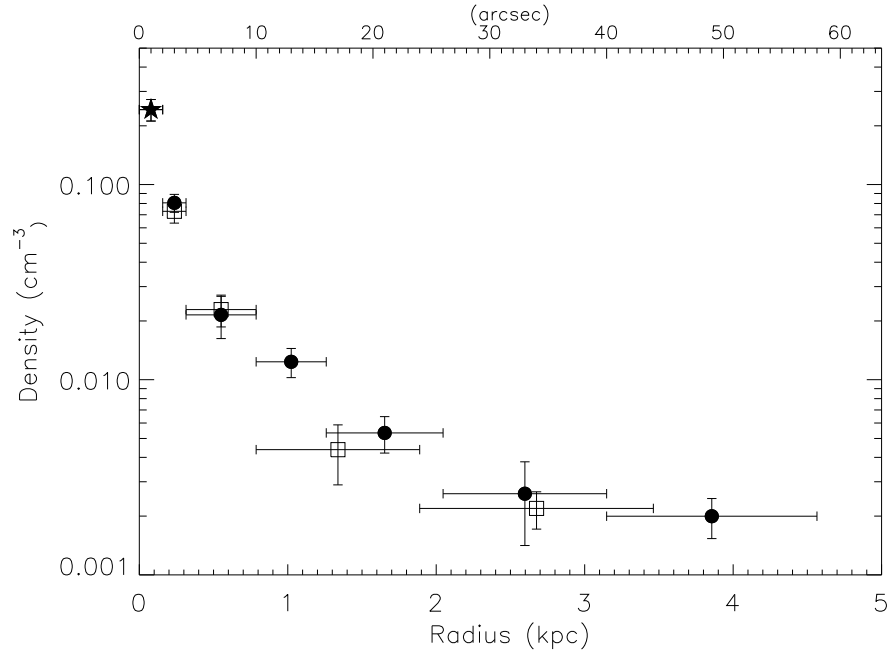


Fig. 7.— Radial distribution of gas density derived from spectral deprojection along two directions (NE–SW, filled circles; and NW–SE, open boxes). The density for the inner 2'' derived using only the last two observations is shown as a star. See Sect. 4.2 for more details.

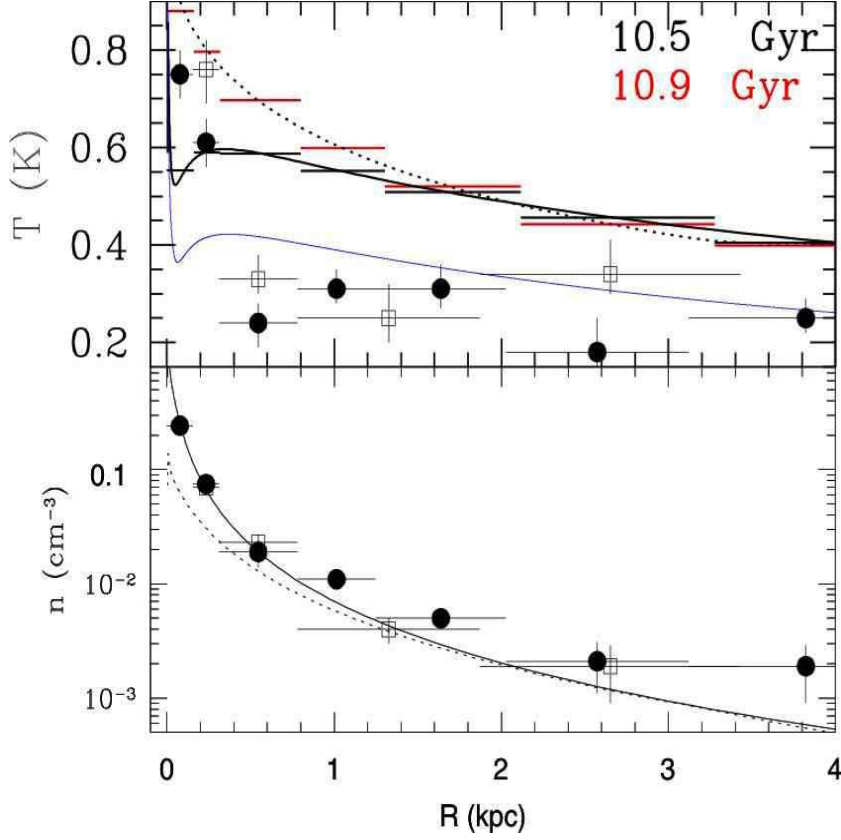


Fig. 8.— The 3D radial temperature profile (upper panel) and density profile (lower panel) for the observed values (full circles and open squares, respectively for the NE-SW and NW-SE quadrants), and for the representative model presented in the Appendix and discussed in Sect. 5.2.1, at two epochs: 10.5 Gyr (solid line) and 10.9 Gyr (dotted line). The model temperature at these epochs is also shown with bars, calculated by averaging the temperature with the 0.3–8 keV emission over bins of a width as much as possible close to that used for the observed data (compatibly with the spacing of the numerical grid). The blue line shows the heating due to stellar motions $T_\sigma(r)$; note the central spike due to the MBH. See Sect. 5.2.1 and the Appendix for more details.

Table 1: General properties of NGC4278

D (Mpc)	Morph. type	B_0^T (Bmag)	$L_B/10^{10}$ ($L_{B,\odot}$)	Optical class	M_{BH} ($10^8 M_\odot$)	$\sigma_{e/8}$ (km s $^{-1}$)	R_e (")
(1)	(2)	(3)	(4)	(5)	(6)	(7)	(8)
16.1	E1+	10.97	1.7	L1.9	3.4	252	32

Col. 1: distance from Tonry et al. (2001); cols. 2 and 3: morphological type and B_0^T from RC3; col. 4: L_B from B_0^T and the adopted distance; col. 5: type of optical nuclear emission (Ho et al. 1997); col. 6: M_{BH} from the $M_{BH} - \sigma$ relation (Tremaine et al. 2002); col. 7: stellar velocity dispersion within a central aperture of $R_e/8$ (Kuntschner et al. 2010); col. 8: effective radius (Cappellari et al. 2006).

Table 2. Summary of Nuclear Flux Variations

ObsId	Date	Γ	$F_{0.5-8\text{ keV}}$	$L_{0.5-8\text{ keV}}$
XMM-Newton	2004 May 23	2.05 [2.03-2.07]	33.8 [32.8-34.2]	10.70 [10.61-10.80]
Chandra 4741	2005 Feb 02	2.13 [2.00-2.28]	18.1 [17.1-18.8]	5.74 [5.65-6.24]
Chandra 7077	2006 Mar 16	2.26 [2.16-2.39]	7.8 [7.5-7.9]	2.55 [2.48-2.79]
Chandra 7078	2006 Jul 25	2.34 [2.22-2.47]	16.0 [14.9-16.2]	5.12 [4.99-5.74]
Chandra 7079	2006 Oct 24	2.38 [2.28-2.50]	14.1 [13.3-14.3]	4.67 [4.56-5.09]
Chandra 7081	2007 Feb 20	2.12 [2.00-2.25]	6.2 [5.9-6.4]	1.99 [1.92-2.20]
Chandra 7080	2007 Apr 20	2.02 [1.84-2.20]	5.9 [5.5-6.1]	1.86 [1.77-2.11]
Chandra 11269	2010 Mar 15	2.31 [2.11,2.51]	1.09 [0.98-1.15]	0.36 [0.35-0.38]
Chandra 12124	2010 Mar 20	2.31 [2.11,2.51]	0.94 [0.65-1.01]	0.29 [0.27-0.32]

Note. — Γ is the photon index of the nuclear power law component; $F_{0.5-8\text{ keV}}$ is the observed flux in units of 10^{-13} erg cm $^{-2}$ s $^{-1}$; $L_{0.5-8\text{ keV}}$ is the intrinsic luminosity in units of 10^{40} erg s $^{-1}$. Compiled from measurements in Younes et al. (2010) and this work.

Table 3. X-ray Spectral Properties of the nucleus from the 2010 *Chandra* observations

N_H (cm $^{-2}$)	kT (keV)	Γ	$L_{0.5-8\text{ keV}}$ (erg s $^{-1}$)	$L_{APEC,0.5-8\text{ keV}}$ (erg s $^{-1}$)	$L_{POW,0.5-8\text{ keV}}$ (erg s $^{-1}$)	$L_{0.5-2\text{ keV}}$ (erg s $^{-1}$)	$L_{2-10\text{ keV}}$ (erg s $^{-1}$)
4.18 ± 3.13	0.75 ± 0.05	2.31 ± 0.20	3.5E+39	1.0E+39	2.5E+39	2.5E+39	1.1E+39

Note. — Luminosities are corrected for an absorption column of $N_H = 4.18 \times 10^{20}$ cm $^{-2}$; they refer to the total emission in the given band, when the spectral component is not specified.

Table 4. Best-Fit Parameters for the Spectral Modeling with Deprojection

Annuli (arcsec)	N_H (10^{20} cm $^{-2}$)	kT (keV)	$Norm_{kT}$	Γ	$Norm_\Gamma$
Nucleus (ObsID 11269,12124)			($\chi^2/\text{dof}=124.8/101$)		
0–2	4.18 ± 3.13	0.75 ± 0.05	$1.1E-5 \pm 1.3E-6$	2.31 ± 0.20	$2.1E-5 \pm 3.4E-6$
NE–SW (All ObsIDs)			($\chi^2/\text{dof}=692.8/616$)		
2–4	1.76	0.61(–0.05, +0.05)	$3.5E-6 \pm 3.6E-7$	1.8	$4.5E-6 \pm 4.1E-7$
4–10	1.76	0.24(–0.05, +0.04)	$2.5E-6 \pm 6.0E-7$	1.8	$1.6E-6 \pm 3.3E-7$
10–16	1.76	0.31(–0.03, +0.04)	$4.0E-6 \pm 6.8E-7$	1.8	$1.5E-6 \pm 4.3E-7$
16–26	1.76	0.31(–0.04, +0.05)	$3.6E-6 \pm 7.6E-7$	1.8	$2.0E-6 \pm 5.5E-7$
26–40	1.76	0.18(–0.10, +0.07)	$3.0E-6 \pm 1.4E-6$	1.8	$2.3E-6 \pm 6.9E-7$
40–58	1.76	0.25(–0.03, +0.04)	$5.1E-6 \pm 1.2E-6$	1.8	$2.1E-6 \pm 8.3E-7$
NW–SE (All ObsIDs)			($\chi^2/\text{dof}=409.5/350$)		
2–4	1.76	0.76(–0.07, +0.06)	$3.0E-6 \pm 3.9E-7$	1.8	$3.8E-6 \pm 4.6E-7$
4–10	1.76	0.33(–0.03, +0.05)	$3.3E-6 \pm 6.0E-7$	1.8	$3.2E-6 \pm 4.0E-7$
10–24	1.76	0.25(–0.05, +0.07)	$2.1E-6 \pm 7.1E-7$	1.8	$3.3E-6 \pm 5.2E-7$
24–44	1.76	0.34(–0.04, +0.07)	$3.3E-6 \pm 7.2E-7$	1.8	$3.0E-6 \pm 7.1E-7$

Note. — Outside the nucleus, the fit required a very small absorption column ($N_H < 10^{20}$ cm $^{-2}$), thus N_H was fixed at the line-of-sight Galactic value towards NGC 4278 ($N_H = 1.76 \times 10^{20}$ cm $^{-2}$, from the CXC tool COLDEN); also, the power-law Γ was fixed at 1.8 to account for unresolved LMXBs. Solar abundance was assumed for the thermal component in all fits. Only one χ^2/dof is given for the series of annuli in each direction, because the spectral fitting was done simultaneously for the annuli.

Table 5. Derived Physical Parameters for the Hot Gas Component

Annuli (arcsec)	n_e (cm^{-3})	p (dyne cm^{-2})	E_{th} (erg)	L_{apec} (erg s^{-1})	M_{hot} ($10^5 M_\odot$)
Nucleus (ObsID 11269,12124)					
0–2	0.242 ± 0.030	5.8E-10	4.1E+53	1.0E+39	1.0
NE–SW (All ObsIDs)					
2–4	0.072 ± 0.008	1.4E-10	4.0E+53	1.6E+38	1.1
4–10	0.019 ± 0.005	1.5E-11	6.9E+53	3.5E+38	5.0
10–16	0.011 ± 0.002	1.1E-11	1.7E+54	1.7E+38	9.6
16–26	0.005 ± 0.001	4.7E-12	3.1E+54	1.2E+38	18.0
26–40	0.002 ± 0.001	1.4E-12	3.2E+54	8.5E+37	30.3
40–58	0.002 ± 0.001	1.4E-12	9.2E+54	8.4E+37	65.5
NW–SE (All ObsIDs)					
2–4	0.073 ± 0.009	1.8E-10	4.0E+53	9.7E+37	0.9
4–10	0.023 ± 0.004	2.4E-11	9.1E+53	1.9E+38	4.8
10–24	0.004 ± 0.001	3.6E-12	1.8E+54	8.7E+37	12.6
24–44	0.002 ± 0.001	2.3E-12	6.7E+54	6.8E+37	35.0

Note. — The electron number densities were derived from the emission measure for the thermal component. Luminosities are reported for the 0.5–8 keV range, and are absorption corrected ($N_H = 1.76 \times 10^{20} \text{ cm}^{-2}$).

7. Appendix

The hot gas flow in NGC4278 has been investigated in Sect. 5.2.1 with spherically symmetric hydrodynamical simulations following the evolution of the stellar mass losses from a single burst passively evolving stellar population. This is a reasonable model thanks to the regular optical appearance of NGC4278, a roundish galaxy with a uniformly old stellar population (see the Introduction). The galaxy model for the simulations, including a central black hole, a stellar and a dark mass components, was built as follows. The stellar density was derived from the surface brightness profile in the I band from *HST* WFPC2 *F814W* images and large-field ground-based photometry (Cappellari et al. 2006). This profile extends from $152''$ down to $R \approx 0.05''$, within which the optical AGN dominates; within a radius of $1''$ the profile flattens in a core; the effective radius is $R_e = 32''$ (equivalent to 2.496 kpc). For the distance adopted here, the I -band luminosity is $L_I = 3.4 \times 10^{10} L_{\odot, I}$, using the total observed magnitude $I_T = 8.83$, after correction for extinction (Cappellari et al. 2006). By spherical deprojection of this surface brightness profile we derived the 3D radial trend of the stellar density profile. The adopted central stellar velocity dispersion σ_0 was the observed luminosity weighted velocity dispersion within a circular aperture of radius $R_e/8$, that is $\sigma(< R_e/8) = 252 \text{ km s}^{-1}$ (Kuntschner et al. 2010; Tab. 1). In the modeling of the total mass distribution, we imposed this σ_0 value to the projected and luminosity-weighted average of the stellar velocity dispersion within a circle of radius $R_e/8$.

The dark halo was chosen to have a Navarro et al. (1997) profile [$\rho_h \propto 1/(r/r_h)(1 + r/r_h)^2$, with r_h the scale radius, and truncated at large radii], and a total mass M_h . The free parameters M_* , r_h , M_h are determined by imposing the σ_0 value, and the total mass-to-light ratio within R_e derived from models for NGC4278, $M/L_I = 4.5 - 5.2$ (Cappellari et al. 2006), which implies a dark-to-luminous mass ratio within R_e , (\mathcal{R}_e), of $0.5 - 0.7$. By solving numerically the Jeans equations for the three mass components in the isotropic orbits case (e.g., Binney & Tremaine 1987; the stellar velocity dispersion of NGC4278 is nearly isotropic, Cappellari et al. 2007), with a central MBH acting as a point mass of $M_{BH} = 3.4 \times 10^8 M_{\odot}$ (Tab. 1), the resulting model has a stellar mass-to-light ratio of $M_*/L_I = 4.0$, $\mathcal{R}_e = 0.69$, $\mathcal{R} = M_h/M_* = 3.5$ (in good agreement with the value at $10R_e$ of ~ 3 from Bertola et al. 1993, Kronawitter et al. 2000). Figure 9 shows the main dynamical properties of the adopted mass model.

The time evolving input ingredients of the simulations are the rate of stellar mass loss from the aging stellar population (\dot{M}_*), and the rate of SNIa heating (L_{SN}). The mass return rate prescribed by the stellar evolution theory is used, as well as its decline as a function of time, computed following the prescriptions of Maraston (2005) for solar abundance and the Kroupa IMF (e.g., Pellegrini 2012). The present-epoch SNIa's rate for nearby early-type

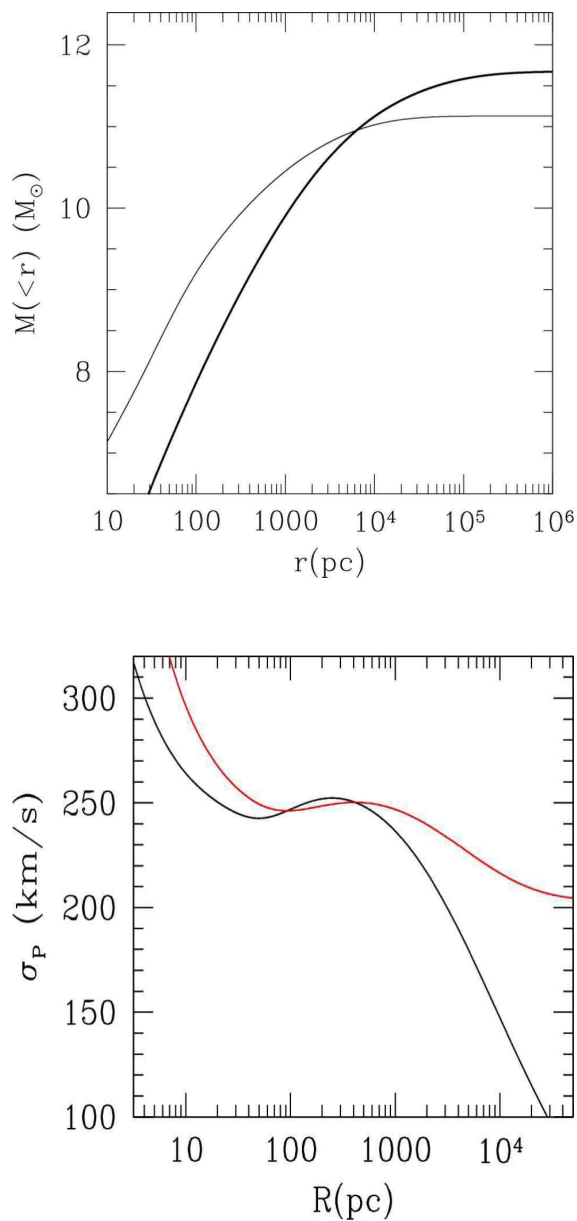


Fig. 9.— Top: the mass profile for the adopted galaxy model (thicker line for the dark mass, thinner one for the stellar mass). Bottom: the model projected stellar velocity dispersion, in black, and the aperture velocity dispersion, in red. Note how the red curve reaches the aperture velocity dispersion of 252 km s^{-1} at $R_e/8$ (and of $231 \pm 5\% \text{ km s}^{-1}$ at R_e , as observed by Kuntschner et al. 2010); note also the central increase produced by the MBH.

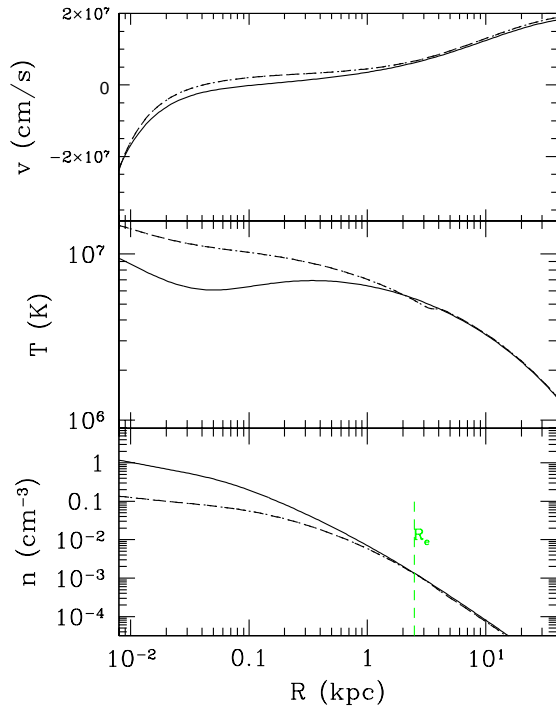


Fig. 10.— Radial trend of the main hydrodynamical quantities of the gas flow for the representative model described in the Appendix and discussed in Sect. 5.2.1; displayed are the velocity (negative inward), top; the temperature, middle; the gas number density, bottom, for a galaxy age of 10.5 (solid) and 10.9 (dot-dashed) Gyr.

galaxies is adopted, i.e., $0.16h_{70}^2$ SNu (where 1 SNu = 1 SNIa per 100 yr per $10^{10}L_{B,\odot}$, $h_{70} = H_o/70$; Cappellaro et al. 1999; Li, W. et al. 2011). The secular evolution of the rate is taken as $\propto t^{-s}$, with $s = 1.1$, as suggested by recent large supernova surveys and modeling (e.g., Maoz et al. 2011). Another source of heating for the stellar mass losses is the thermalization of the stellar random motions, that corresponds to a gas mass-weighted temperature of $T_\sigma = \frac{1}{k} \frac{\mu m_p}{M_*} \int 4\pi r^2 \rho_*(r) \sigma^2(r) dr$, where k is the Boltzmann constant, μm_p the mean particle mass, $\sigma(r)$ is the one-dimensional velocity dispersion of the stars, and $\rho_{gas}(r) \propto \rho_*(r)$ is assumed, where $\rho_*(r)$ is the stellar density profile (see Pellegrini 2012 for more details).

The evolution of the galactic gas flow is obtained integrating the time-dependent Eulerian equations of hydrodynamics with the above described source terms, with a numerical code described in Pellegrini (2012), with a sink of the hydrodynamical quantities at the galactic center, and no feedback effects from the central MBH. We adopt a central grid spacing of 5 pc for a good sampling of the inner regions, even within the Bondi radius, and a total of 240 logarithmically spaced gridpoints. The simulations begin at an age of 2 Gyr for the stellar population, when the galaxy has completed its formation process and the galactic wind phase driven by type II supernovae explosions has already started, and end at the age of NGC4278, 10.7 ± 2.14 (Terlevich & Forbes 2002). Figure 10 shows the radial profiles of the main hydrodynamical quantities (velocity, temperature and density) at the two epochs considered for Fig. 8.